

**UCLA**

**UCLA Electronic Theses and Dissertations**

**Title**

Application of Coupled Modes in Compact Antenna and Reflector Array

**Permalink**

<https://escholarship.org/uc/item/8tb9x1zw>

**Author**

Tian, Haozhan

**Publication Date**

2020

Peer reviewed|Thesis/dissertation

UNIVERSITY OF CALIFORNIA

Los Angeles

Application of Coupled Modes in Compact Antenna and Reflector Array

A dissertation submitted in partial satisfaction  
of the requirements for the degree  
Doctor of Philosophy in Electrical and Computer Engineering

by

Haozhan Tian

2020

© Copyright by

Haozhan Tian

2020

# ABSTRACT OF THE DISSERTATION

Application of Coupled Modes in Compact Antenna and Reflector Array

by

Haozhan Tian

Doctor of Philosophy in Electrical and Computer Engineering

University of California, Los Angeles, 2020

Professor Tatsuo Itoh, Chair

Compact antenna has been widely used due to its advantage of compact size and low fabrication cost. With the development of communication, antennas with unique radiation features are required for different scenarios. For example, beam steering is desired for 5G; while endfire radiation is for vehicle-to-vehicle communications. These requirements bring new challenges to the design of the compact antenna. In order to realize the features, designers always have to compromise on size, robustness, or fabrication cost. To alleviate this problem, we propose a new design method that applies coupled modes into the compact antenna designs. In this dissertation, beam steering antenna, endfire antenna with vertical polarization, and circularly-polarized antenna are demonstrated respectively. All the proposed antennas remain compact, robust, and cost-efficient. In addition, the coupled-mode concept is further extended to design reflector array. The proposed retro-reflective grating array works for wide-band incoming wave with any polarization. Other possible applications of the proposed concept are also discussed.



The dissertation of Haozhan Tian is approved.

Benjamin Williams

Mona Jarrahi

Yuanxun Ethan Wang

Tatsuo Itoh, Committee Chair

University of California, Los Angeles

2020

*To my parents,  
for their love and whip.  
To my lovely wife and daughter,  
for completing my life.*

## TABLE OF CONTENTS

<b>1</b>	<b>Introduction</b> . . . . .	<b>1</b>
<b>2</b>	<b>Introduction to Coupled Mode Patch Antenna</b> . . . . .	<b>3</b>
2.1	Introduction . . . . .	3
2.2	Beam Scanning Using Mutual Coupling . . . . .	4
2.2.1	Operation . . . . .	5
2.2.2	Design from a Filtering Antenna Perspective . . . . .	6
2.3	Simulation and Measurement . . . . .	8
2.4	Conclusion . . . . .	12
<b>3</b>	<b>Fixed-Frequency Wide-Range Beam Scanning CMPA</b> . . . . .	<b>14</b>
3.1	Introduction . . . . .	14
3.2	Antenna Design and Operation . . . . .	15
3.3	Simulation and Measurement . . . . .	19
3.3.1	Performance with Varactor SMV1413 . . . . .	20
3.3.2	Wide-Angle Scanning Realized by Varactor SMV1405 . . . . .	23
3.4	Conclusion . . . . .	28
<b>4</b>	<b>Endfire CMPA with Vertical Polarization</b> . . . . .	<b>30</b>
4.1	Introduction . . . . .	30
4.2	Design and Operation . . . . .	32
4.2.1	Model of Two-Element Array . . . . .	33
4.2.2	Finite Ground Plane Effect . . . . .	37
4.2.3	Circuit Model . . . . .	38
4.3	Simulation and Measurement . . . . .	39

4.4	Discussion . . . . .	43
4.5	Conclusion . . . . .	44
<b>5</b>	<b>Circularly Polarized HMSIW Antenna . . . . .</b>	<b>46</b>
5.1	Introduction . . . . .	46
5.2	Design Method and Theory . . . . .	47
5.2.1	Design Procedure . . . . .	48
5.2.2	Mode Analysis . . . . .	51
5.3	Antenna Results . . . . .	53
5.4	Conclusion . . . . .	55
<b>6</b>	<b>Wide-Band Blazed Grating for All Polarization . . . . .</b>	<b>57</b>
6.1	Introduction . . . . .	57
6.2	Operation Mechanism . . . . .	59
6.2.1	Grating Equation and Bragg Condition . . . . .	59
6.2.2	Unit Cell . . . . .	60
6.3	Wide-band Blazed Grating . . . . .	62
6.3.1	Simulation . . . . .	62
6.3.2	Measurement . . . . .	65
6.4	Conclusion . . . . .	65
<b>7</b>	<b>Conclusion . . . . .</b>	<b>67</b>
	<b>References . . . . .</b>	<b>71</b>

## LIST OF FIGURES

1.1	(a) Beam steering antenna for 5G. (b) Endfire radiation for vehicle-to-vehicle communication. . . . .	1
2.1	Schematic of the proposed design. (a) Top view. The black dots are the metal via connecting top metal to the ground. The dimensions are all in mm: $l = 9.5$ , $\Delta l = 0.5$ , $w = 28$ , $s = 3.5$ . The height of the board is $h = 0.79$ mm. The diameter of the via is 0.8 mm and the spacing is 1.6 mm. (b) Side view. (c) Front view. . . . .	4
2.2	The demonstration of coupled E field distribution in symmetric structure at (a) even mode and (b) odd mode. The dash line represents the via wall with a open gap for coupling. . . . .	5
2.3	Equivalent lumped circuit model where radiation loss of the two cavities are represented by $G_1$ and $G_2$ , respectively. Parameters: $G_0 = 0.02 S$ , $J_{0,1} = 1.035 \times 10^{-2} S$ , $L_1 = 0.278$ nH, $C_1 = 3.575$ pF, $G_1 = 4.040 \times 10^{-3} S$ , $J_{1,2} = 3.938 \times 10^{-3} S$ , $L_2 = 0.264$ nH, $C_2 = 3.771$ pF, $G_2 = 3.856 \times 10^{-3} S$ . . . . .	7
2.4	(a) The simulated, measured, and circuit-model $S_{11}$ response. (b) Fabricated Sample of the proposed antenna. . . . .	8
2.5	Simulated vector distribution of the electric field in the substrate on the cross section. Three frequencies refer to even mode, the mode at the intermediate peak frequency, and odd mode. . . . .	9
2.6	Simulated co-polarized radiation patterns on E plane. The patterns are normalized to 1 and shown in absolute value. . . . .	9
2.7	Realized boresight gain versus frequency. The measured gains, shown in this figure, are at 4.975 GHz, 5.03 GHz, 5.12 GHz, and 5.165 GHz respectively. . . .	10
2.8	Simulated and measured radiation patterns on E plane at (a) 4.975 GHz (even mode), (b) 5.03 GHz (90° out of phase), and (c) 5.12 GHz (odd mode). The simulated cross-pol level is below the minimum scale -30 dB. . . . .	11

2.9	Measured realized gain patterns in absolute value on E plane. . . . .	12
3.1	Schematic of the proposed antenna. (a) Top view. (b) Bottom view including the contour of the top patch. (c) Loaded slot. . . . .	14
3.2	(a) Simulated frequency response of the antenna under different capacitances of the varactor $C_v$ . The E and H field distributions in the cavity at (b) low frequency pole 2.301 GHz and (c) high frequency pole 2.363 GHz when $C_v = 0.5$ pF; at (d) low frequency pole 2.348 GHz and (e) high frequency pole 2.387 GHz when $C_v = 3$ pF. The varactor is simply modeled by a pure capacitor that is defined by RCL Boundary Condition in HFSS®. . . . .	16
3.3	(a) Simulated frequency response perturbed by the slot resonance during the transition from capacitive to inductive. The poles pointed by black arrows are corresponding to the slot resonance, whose E and H field distributions at (b) 2.157 GHz when $C_v = 2$ pF, and (c) 2.638 GHz when $C_v = 1.5$ pF are plotted. . . . .	18
3.4	Fabricated sample of (a) top view, (b) bottom view, and (c) zoomed view for the loaded slot. . . . .	20
3.5	(a) Simulated frequency response under tuning of varactor SMV1413. The inset figure shows the equivalent circuit model of varactor, where the series inductance $L_s = 0.7$ nH, series resistance $R_s = 0.35\Omega$ , parallel capacitance $C_p = 0.3$ pF, and junction capacitance $C_J$ is tuned. (b) Measured frequency response under different bias voltages ( $V_b$ ) for varactor SMV1413. . . . .	21
3.6	(a) Measured E-plane co-polarized radiation patterns under different bias at 2.35 GHz. The patterns are normalized and plotted in dB scale. (b) Measured peak gain and total efficiency of the antenna versus bias voltage at 2.35 GHz. . . . .	21
3.7	Measured co-polarized realized gain patterns under different bias at 2.3 GHz on E plane. . . . .	23
3.8	Comparison of the measured frequency response for the antenna loaded by two varactors respectively. . . . .	24

3.9	(a) Simulated frequency response under different junction capacitance in the resonant range. The values of the circuit model for SMV1405 are $L_s = 0.7$ nH, $R_s = 0.8\Omega$ , and $C_p = 0.29$ pF. (b) Measured frequency response under different bias in the resonant range. . . . .	25
3.10	Measured frequency response under different bias in (a) the transition (resonant) range and (b) the inductive range. . . . .	25
3.11	Measured co-polarized realized gain patterns on E plane under different bias at 2.29 GHz. The antenna is loaded with varactor SMV1405 only. . . . .	26
3.12	Measured peak gain and total efficiency of the antenna versus bias voltage at 2.29 GHz. . . . .	28
4.1	Schematic of the proposed design. (a) Top view. The black dots represent the metal via posts, with diameter of 1.6 mm and spacing of 3.2 mm, connecting top patch to the ground. The dimensions are all in mm: $l = 16.5$ , $l_t = 33$ , $w = 55$ , $g = 5$ . (b) Bottom view. The ground metal and the substrate have same size as the top patch, $l_g = l_t$ . The gray hole is the etched out of the ground for the feeding coaxial waveguide, whose inner diameter is 1.27 mm and outer diameter is 4.1 mm. The center of the feeding is located at $s = 5$ mm. (c) Back view. The antenna is back-fed from bottom. . . . .	31
4.2	The demonstration of the E field vector distribution in the coupled cavity for (a) even mode and (b) odd mode. . . . .	31
4.3	Pattern of even and odd mode calculated by Eq. (4.1) with additional phase shift of (a) $\phi_1 = 0^\circ$ and (b) $\phi_1 = 60^\circ$ . . . . .	33
4.4	Simulated frequency responses of the antenna with different excitation locations, where $s$ is the distance between the center via wall and the feeding pin as shown in Fig. 4.1. . . . .	34
4.5	Simulated radiation patterns of the antenna with different excitation locations at even-mode pole on $xz$ plane of cut. . . . .	35

4.6	Equivalent lumped circuit model of the proposed antenna, where $G_0 = 0.02 S$ stands for source, $J_{01} = 1.23 \times 10^{-3} S$ for external coupling, $J_{12} = 3.6 \times 10^{-4} S$ for internal coupling, $L_1 = 0.45 \text{ nH}$ and $C_1 = 9.67 \text{ pF}$ for each of the half cavities, and $G_1 = 2.17 \times 10^{-3} S$ for the radiation loss. . . . .	37
4.7	Simulated co-polarized normalized patterns of the antenna on (a) Elevation ( $xz$ ) plane and (b) Azimuth ( $xy$ ) plane for different frequencies. The direction angles are $\theta$ in (a) and $\phi$ in (b). . . . .	38
4.8	The fabricated antenna fed via a quarter-wavelength bazooka balun from (a) top view and (b) side view with the balun zoomed in. . . . .	39
4.9	The simulated and measured $S_{11}$ response for the antenna with balun. The measured result of the antenna without balun is also plotted as a reference. . .	40
4.10	Measured and simulated normalized patterns for the antenna with balun on (a) Elevation ( $xz$ ) plane and (b) Azimuth ( $xy$ ) plane at even mode 2.40 GHz, intermediate frequency 2.41 GHz, and odd mode 2.425 GHz. . . . .	41
4.11	Measured and simulated forward endfire realized gain and F/B ratio versus frequency. . . . .	42
4.12	Measured and simulated total efficiency of the antenna versus frequency. . . .	43
5.1	Top-view schematic layout of the proposed filtering antenna. The black dots represent the metal via posts connecting top to the ground, whose diameter is 1.6 mm and spacing is 3.2 mm. The red dot is the back-fed probe. The dimensions are all in mm: $l = 38.9$ , $g = 7.5$ , $s = 4$ . . . . .	47
5.2	(a) HMSIW radiating resonator. (b) Equivalent lumped circuit model for the radiating resonator. . . . .	48
5.3	Equivalent circuit model loaded with (a) the radiation conductance $G_r$ , and (b) the standard loads $G_{L1} = G_{L2} = 0.02 S$ . The admittance inverters $J_{1L}$ and $J_{2L}$ are inserted in (b), such that $Y_1 = Y_2 = G_r$ . The values are: $G_0 = 0.02 S$ , $J_{01} = 1.29 \times 10^{-3} S$ , $J_{12} = 3.58 \times 10^{-4} S$ , $L_1 = L_2 = 0.42 \text{ nH}$ , $C_1 = C_2 = 4.71 \text{ pF}$ , $G_r = 2.98 \times 10^{-3} S$ , and $J_{1L} = J_{2L} = 1.07 \times 10^{-3} S$ . . . . .	49



5.4	Frequency response of the circuit model shown in Fig. 5.3 (b), where $G_0$ , $G_{L1}$ , and $G_{L2}$ refer to Port 1, 2, and 3 respectively. . . . .	50
5.5	Simulated distributions of the complex E field magnitude at (a) even mode and (b) odd mode, and the surface J vector at (c) even mode and (d) odd mode.	52
5.6	Simulated and measured (a) $S_{11}$ response and (b) Axial Ratio (AR) of the proposed antenna at broadside. The inset figure in (a) shows the fabricated sample. . . . .	53
5.7	(a) Simulated distribution of surface J at center frequency. (b) Simulated and measured radiation patterns on $xz$ plane at center frequency. . . . .	54
5.8	Simulated broadside realized gain of RHCP and total efficiency of the proposed antenna. . . . .	55
6.1	(a) A finite grating sample containing 4 by 8 unit cells. The dark and light yellow squares represent the patches in two different sizes. (b) The blazed grating with period $d$ in x direction scatters the incoming wave (blue) to very low specular $m = 0$ reflection (yellow) but strong $m = -1$ diffraction (red). . .	58
6.2	(a) Unit cell settings for perfect auto-collimation at $\theta_i = \theta_{-1} = 30^\circ$ . (b) Top view of the unit cell where two square patches sit on the grounded Rogers RT5880 substrate. . . . .	60
6.3	Simulated frequency responses with TE- and TM-pol excitations for the unit cell. $S_{11}$ stands for specular reflection ( $m = 0$ ) and $S_{21}$ is for $m = -1$ blazing diffraction. . . . .	61
6.4	Simulated complex E-field magnitude distributions under TE-pol excitation at (a) 9.60 GHz and (b) 10.08 GHz, and TM-pol excitation at (c) 9.64 GHz and (d) 10.07 GHz. The contours of the patches are shown by solid black lines. . .	62
6.5	Simulated magnitude of scattering E field at $\theta = \pm 30^\circ$ for (a) TE- and TM-pol; (b) RHCP incident wave at $\theta_i = +30^\circ$ . The specular reflection of a same size PEC mirror is simulated as comparison shown by green slot line. . . . .	63

6.6	Measured auto-collimation results under three incident angles for both TE and TM polarization. The reflection of a same size PEC under normal incident $\theta_i = 0$ is measured to serve as a benchmark. The inset figure shows the fabricated sample. . . . .	64
7.1	(a) Sample of the E-shape CMPA. (b) Frequency response. . . . .	68
7.2	(a) Sample of the two-endfire-element array. (b) Frequency response. Simulated co-pol patterns on (c) Elevation plane and (d) Azimuth plane. . . . .	69

## LIST OF TABLES

4.1	Ground plane effect on the main lobe direction of the proposed antenna . . . .	36
4.2	Comparison of low-profile endfire antennas . . . . .	44
5.1	Comparison of SIW based CP antennas . . . . .	55

## ACKNOWLEDGMENTS

I am so grateful and lucky to meet my advisor, Professor Tatsuo Itoh. He is the lighthouse that navigates my boat towards the scientific research and academia. I greatly admire his dedication to science and kindness to people. It is and will always be an honor be part of Dragon Gate family.

I would like to thank Professor Benjamin Williams, Professor Mona Jarrahi, and Professor Yuanxun Ethan Wang, for their time and efforts being my committee members. I would also like to express my gratitude to Professor Lijun Jiang from University of Hong Kong, for his generous help and contribution to my research. A special thanks to Professor Jing Zhou from Beijing Normal University, who initiated my interest in electromagnetics when I was an undergraduate.

I would like to thank my dearest labmates, Kirti Dhvaj, Xiaoqiang Li and Cheng Tao, for all the patient guidance, heated discussion, and of course, “meaningful” casual chatting. It is the collaboration with you that inspired me and led me where I am now. I am also so grateful to have all my other friends in UCLA, for making my journey full of fun and good memories. Lastly, I would like to thank my beautiful, smart and lovely wife, for her company and support. You bring the happiness and love to my life that no science could ever fulfill.

## VITA

- 2010-2014    B.S. in Physics, Beijing Normal University, Beijing, China
- 2013-2014    Exchange Student in Ludwig Maximilian University of Munich, Germany
- 2015-2017    M.S. in Electrical and Computer Engineering, University of California Los Angeles, Los Angeles, CA

## PUBLICATIONS

**Haozhan Tian** and Tatsuo Itoh, “Endfire Coupled-Mode Patch Antenna Array with Balanced Feeding”, *IEEE European Microwave Conference (EuMC)*, 2020 (accepted).

**Haozhan Tian**, and Tatsuo Itoh, “Development of a Circularly Polarized HMSIW Antenna”, *Progress In Electromagnetics Research Letters* , 87 (2019): 81-87.

**Haozhan Tian**, Lijun Jiang, and Tatsuo Itoh, “Compact Endfire Coupled-Mode Patch Antenna with Vertical Polarization”, *IEEE Transactions on Antennas and Propagation*, 67.9 (2019): 5885-5891.

**Haozhan Tian**, and Tatsuo Itoh, “Wide-band Blazed Grating for All Polarizations”, *2019 IEEE MTT-S International Microwave Symposium (IMS)*, IEEE, 2019.

**Haozhan Tian**, Lijun Jiang, and Tatsuo Itoh, “A Compact Single-Element Pattern Reconfigurable Antenna with Wide-Angle Scanning Tuned by a Single Varactor”, *Progress In Electromagnetics Research C*, 92 (2019): 137-150.

**Haozhan Tian**, and Tatsuo Itoh, “Coupled-Mode Patch Antenna with Improved Bandwidth and Scanning Angle Range”, *2019 Asia-Pacific Microwave Conference (APMC)*, IEEE, 2019.

**Haozhan Tian**, and Tatsuo Itoh, “All-Polarization Blazed Surface”, *2018 Asia-Pacific Microwave Conference (APMC)*, IEEE, 2018.

**Haozhan Tian**, Kirti Dhvaj, Lijun Jiang, and Tatsuo Itoh, “Beam Scanning Realized by Coupled Modes in a Single Patch Antenna”, *IEEE Antennas and Wireless Propagation Letters*, 17.6 (2018): 1077-1080.

Kirti Dhvaj, **Haozhan Tian**, and Tatsuo Itoh, “Low-Profile Dual-Band Filtering Antenna Using Common Planar Cavity”, *IEEE Antennas and Wireless Propagation Letters*, 17.6 (2018): 1081-1084.

Kirti Dhvaj, Joshua M. Kovitz, **Haozhan Tian**, Lijun Jiang, and Tatsuo Itoh, “Half-Mode Cavity-Based Planar Filtering Antenna With Controllable Transmission Zeroes”, *IEEE Antennas and Wireless Propagation Letters*, 17.5 (2018): 833-836.

**Haozhan Tian**, Mohammad Memarian, and Tatsuo Itoh, “Electronically-tunable resonant blazed metasurface grating”, *2017 Asia-Pacific Microwave Conference (APMC)*, IEEE, 2017.

# CHAPTER 1

## Introduction

Compact antenna typically refers to small-size and low-profile antenna, which still maintains decent radiation efficiency. Examples are planar inverted-F antenna (PIFA), microstrip patch antenna, etc. This type of antenna has been widely used in modern communication systems, due to its advantage of compact size and low fabrication cost. [1]

With the development of communication, antennas with unique radiation features are required for different scenarios. As shown in Fig. 1.1 (a), beam steering antenna is desired for 5G applications; while in Fig. 1.1 (b), endfire antenna is preferred in vehicle-to-vehicle (V2V) communications. These requirements bring new challenges to the design of antenna. Current solutions, such as phased array, always have to compromise on size, robustness, or fabrication cost.

To alleviate this problem, we propose a new design method that applies coupled modes

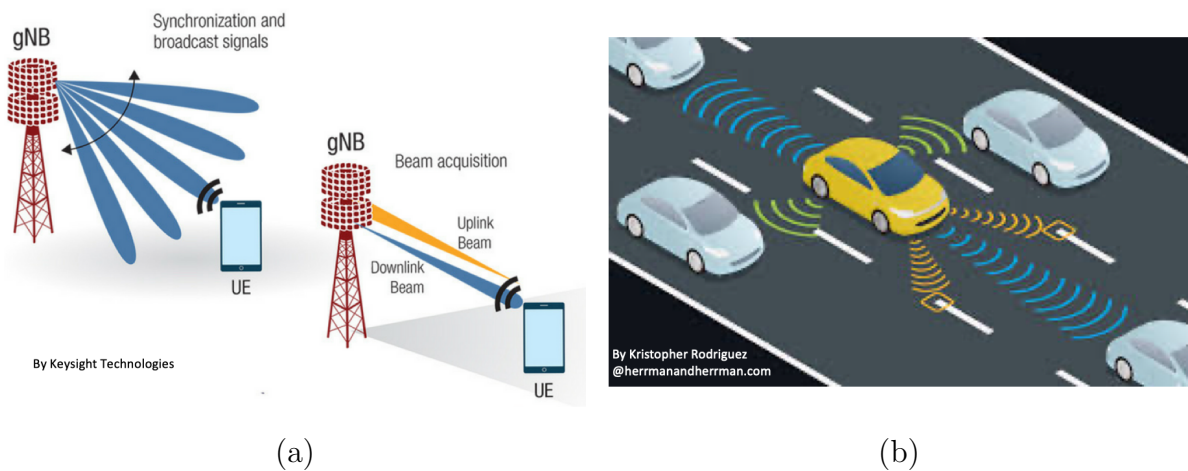


Figure 1.1: (a) Beam steering antenna for 5G. (b) Endfire radiation for vehicle-to-vehicle communication.

into compact antenna designs. Beam steering antenna, endfire antenna with vertical polarization, and circularly-polarized (CP) antenna are realized with the proposed concept and are demonstrated respectively. All the proposed antennas remain compact, robust, and cost-efficient. The coupled-mode concept is further developed and applied to design reflector array. The proposed retro-reflective grating array works for wide-band incoming wave with any polarization.

The dissertation is organized as follows. Chapter 2 demonstrates the operating principle of the proposed method by applying coupled modes into a rectangular patch antenna. The proposed coupled-mode patch antenna (CMPA) steers the beam as a function of frequency. Chapter 3 presents a fixed-frequency beam steering CMPA as a follow-up work. The design achieves wide scanning range and is controlled by only a single varactor diode. Chapter 4 introduces an endfire CMPA with vertical polarization. Chapter 5 is about realizing CP antenna with the proposed method. In Chapter 6, we take the coupling concept beyond compact antenna design and apply it to develop reflective array. A wide-band retro-reflective grating array that works for incoming wave with any polarization is presented. Each chapter has its own background introduction and conclusion for highlighting the contributions.



## CHAPTER 2

### Introduction to Coupled Mode Patch Antenna

#### 2.1 Introduction

Rectangular patch antenna has been widely used in many applications due to its compact configuration, simplicity and low cost [1]. The fundamental mode of operation for this antenna is  $TM_{100}^z$ , which offers the maximum electric fields with  $180^\circ$  phase difference at two radiating slots. The radiation mechanism of patch antenna has been typically explained from two perspectives. In transmission-line model, the radiation is from the fringing fields at two radiation slots. In cavity model, it is from two in-phase equivalent magnetic currents. Derived from either of the explanations, the radiation pattern of patch antenna is basically independent on the frequency as long as the operation mode remains same.

Beam steering antennas, on the other hand, are desired for many applications. A good example is the leaky-wave antenna whose beam pattern scans in the space as the operating frequency changes [2]. The radiation for this type of antenna is realized by leaking energy gradually as the wave propagating along the structure. The beam scanning angle is determined by the frequency dependent propagation constant [3]. In order to maintain a high radiation efficiency, the antenna has to be longer than one wavelength in general. Another way is to use the phased array [4]. The beam scanning is realized by properly tuning the phase and amplitude of each element. However, the structure of an array can be bulky and complex.

In this chapter, we introduce coupled modes in a patch antenna to realize beam scanning [5]. The phase difference of two radiation slots can be manipulated by the design. The beam scans from broadside to  $43^\circ$  within 3-dB realized boresight gain bandwidth in

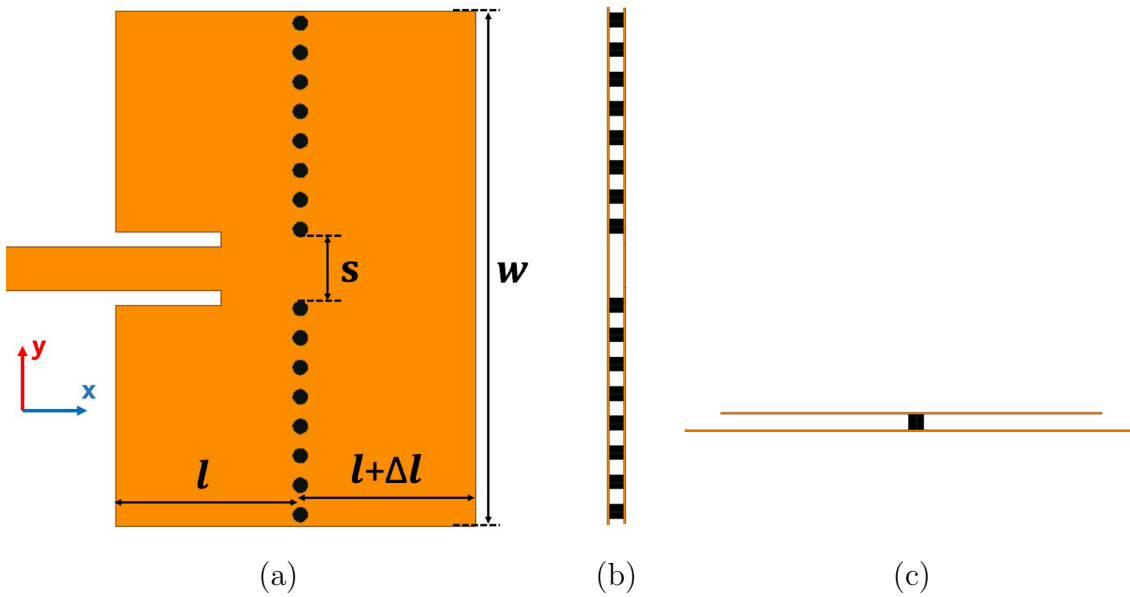


Figure 2.1: Schematic of the proposed design. (a) Top view. The black dots are the metal via connecting top metal to the ground. The dimensions are all in mm:  $l = 9.5$ ,  $\Delta l = 0.5$ ,  $w = 28$ ,  $s = 3.5$ . The height of the board is  $h = 0.79$  mm. The diameter of the via is 0.8 mm and the spacing is 1.6 mm. (b) Side view. (c) Front view.

simulation. The implemented sample realizes 4.55% 10-dB bandwidth of  $S_{11}$  with center frequency at 5.05 GHz by measurement. The design shares the simple and compact configuration of patch antenna, while maintaining a high radiation efficiency in the meantime. The operation mechanism along with the results of simulation and measurement is presented in the following sections.

## 2.2 Beam Scanning Using Mutual Coupling

The schematic of the proposed antenna is illustrated in Fig. 2.1. A ground-backed Rogers RT/Duroid 5880 substrate is used for the design, with dielectric constant of 2.2, loss tangent of 0.001, and height 0.79 mm. The antenna is based on a rectangular patch antenna with an inset feed line. The size of the antenna is characterized by the width  $w$  and total length  $l_{total} = 2l + \Delta l$ . Metallic via posts are inserted around the center, connecting the top patch with the ground. These via posts behave like a metallic wall for

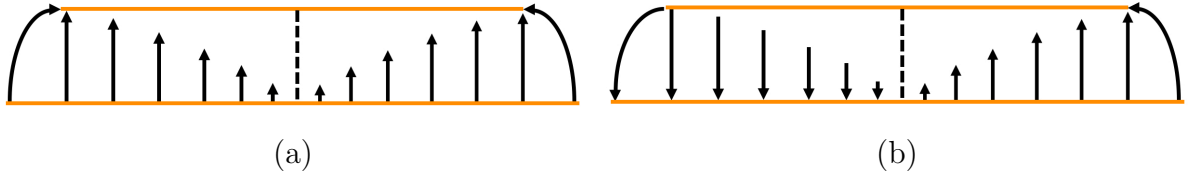


Figure 2.2: The demonstration of coupled E field distribution in symmetric structure at (a) even mode and (b) odd mode. The dash line represents the via wall with a open gap for coupling.

the EM field in the substrate, which divide the patch cavity into two parts. Each part is a resonator which supports a half mode of  $TM_{100}$ . A gap with the width of  $s = 3.5$  mm is opened on the interior wall by removing some via posts. It functions as a coupling iris.

### 2.2.1 Operation

The mutual coupling between two cavities results in two eigen-mode solutions, which are called even mode and odd mode, respectively. For simplicity, let us first analyze a symmetric structure as shown in Fig. 2.2, where the dash line is at the center and thus the two half-mode cavities are identical. The E field distributions of even and odd mode are demonstrated in Fig. 2.2 (a) and (b) respectively. The structure can then be modeled by an array of two equivalent magnetic currents with the same amplitude but different phases. In  $x$ - $z$  plane, the array factor (AF) is given by [1]

$$AF = 2 \cos \left[ \frac{1}{2} (k_0 d \sin \theta + \Delta\phi) \right] \quad (2.1)$$

where  $k_0$  is the propagation constant in free space;  $d$  is the separation distance; and  $\Delta\phi$  is the phase difference of the two magnetic currents. The pattern of one of magnetic currents is approximately omnidirectional, and thus beam pattern of the array on E plane is only dependent on AF. In the even mode case where  $\Delta\phi = 180^\circ$ , there will be a null at broadside  $\theta = 0^\circ$  in the far-field pattern due to the out-of-phase cancellation. While for the odd mode where  $\Delta\phi = 0^\circ$ , the structure will radiate like a rectangular patch antenna where the beam peak is at the broadside. As frequencies changing from even to odd

mode, the phase difference  $\Delta\phi$  will gradually shift from  $0^\circ$  to  $180^\circ$  due to the coupling. In consequence, the beam peak will scan away from broadside according to Eq. (2.1).

However, far-field cancellation and two equal lobes in the radiation pattern of even mode are undesired since one main beam scanning around broadside is our goal. Therefore, asymmetry is introduced to the model by putting the metallic via wall slightly off the center so that the two cavities are not identical. In this way, the fields coupling at the iris will pass through different electrical lengths to reach the two radiating edges respectively. Meanwhile, the input feeding brings some phase advance to the left half cavity, which results in extra asymmetry. As a overall result, the phase difference at even mode is close to  $180^\circ$  but not exactly at  $180^\circ$ , which avoids the strong broadside cancellation, and leads to one main beam instead of two equal lobes at even mode. In the meantime, the beam peak also shifts slightly away from the broadside at odd mode due to the asymmetry. The even mode or odd mode is defined by the type of coupling that happens at the iris, not by the phase difference between the two radiation slots. That means the even and odd modes are still two eigen-mode solutions of an asymmetric model. It has to be mentioned that there will still be a minor lobe and a null in the radiation pattern scanning with frequency as predicted by Eq. (2.1). In fact, we may benefit from the scanning null in some applications like cognitive radio. We will leave this discussion for the future.

### 2.2.2 Design from a Filtering Antenna Perspective

The design philosophy is borrowed from the procedure to design a filtering antenna [6]. The idea is first to generate a circuit model to meet desired operation frequency and bandwidth, as the design procedures of a two-pole passband filter. In this way, we can determine how fast the beam scans with frequency, and get reasonable realized boresight gain within the band. Unlike traditional two-port filter, the model of the proposed design is built with only source port but no load port. This is because the input energy will be radiated out directly to the free space, instead of to a load port as the traditional two-port passband filter. Therefore, in the model, the radiation conductance of the antenna is regarded as equivalent load.

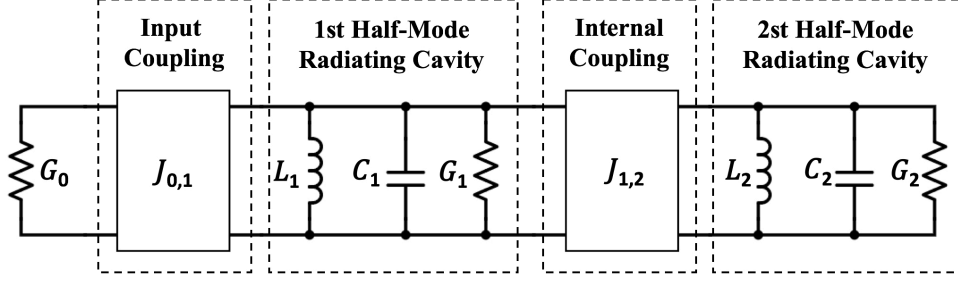


Figure 2.3: Equivalent lumped circuit model where radiation loss of the two cavities are represented by  $G_1$  and  $G_2$ , respectively. Parameters:  $G_0 = 0.02 S$ ,  $J_{0,1} = 1.035 \times 10^{-2} S$ ,  $L_1 = 0.278 \text{ nH}$ ,  $C_1 = 3.575 \text{ pF}$ ,  $G_1 = 4.040 \times 10^{-3} S$ ,  $J_{1,2} = 3.938 \times 10^{-3} S$ ,  $L_2 = 0.264 \text{ nH}$ ,  $C_2 = 3.771 \text{ pF}$ ,  $G_2 = 3.856 \times 10^{-3} S$ .

In Fig. 2.3, the equivalent lumped circuit model is built for a fractional bandwidth of 4.8% at the midband frequency 5.05 GHz. The shunt LC circuits represent the resonance of the two half-mode cavities.  $G_1$  and  $G_2$  stand for the equivalent radiation conductances, which can be theoretically calculated by [1]:

$$G_i = \frac{W}{120\lambda_i} \left[ 1 - \frac{1}{24} \left( \frac{2\pi h}{\lambda_i} \right)^2 \right] \quad (2.2)$$

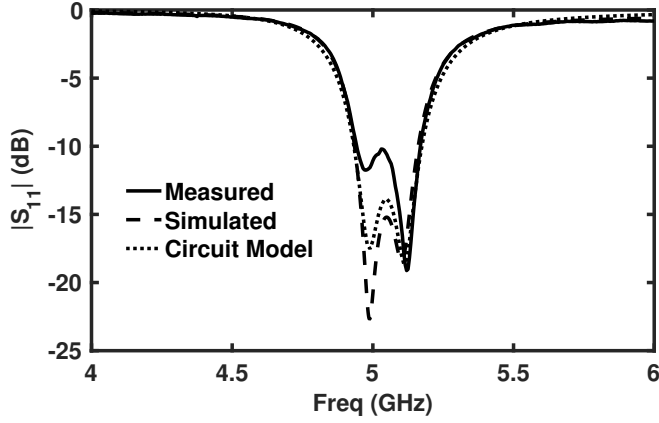
where  $\lambda_i$  is the resonant wavelength in each cavity, for  $i = 1, 2$ . The interstage couplings are modeled by the admittance inverters, whose values are related to external quality factor  $Q_e$  and coupling coefficient  $k$  by

$$Q_e = \frac{b_1 G_0}{J_{0,1}^2} \quad (2.3)$$

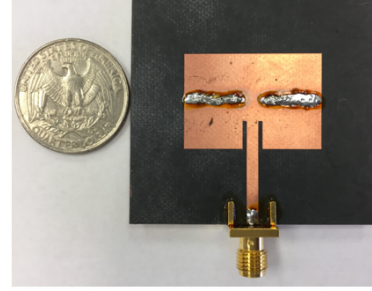
$$k = \frac{J_{1,2}}{\sqrt{b_1 b_2}} \quad (2.4)$$

where  $b_i = 2\pi f_i C_i$  for  $i = 1, 2$ . By applying the methods of filter designs in [7], the parameter values of the model can be calculated. The response of the circuit model is shown in Fig. 2.4 (a) to compare with the one of simulation and measurement.

The structure of the antenna can be designed based on the values of the circuit model. The dimensions of the two half-mode cavities are calculated following similar procedures



(a)



(b)

Figure 2.4: (a) The simulated, measured, and circuit-model  $S_{11}$  response. (b) Fabricated Sample of the proposed antenna.

for designing rectangular patches [1]. Besides the fields of cavity mode, the fringing fields at the radiation slots contribute to the shunt LC circuits in the circuit model as well. The inset feed is designed to guarantee a desired external coupling as indicated in (2.3), which leads to a good input matching. The gap size is determined by the internal coupling coefficient extracted from the circuit model by (2.4). With minor optimization to compensate the inaccuracy of the approximations, the final structure is then designed as shown in Fig. 2.1.

## 2.3 Simulation and Measurement

The simulated, measured, and circuit-model  $S_{11}$  responses match well with each other as shown in Fig. 2.4 (a). The reflection coefficient of the antenna is measured by Agilent 8510C Vector Network Analyzer. The measured center frequency is 5.05 GHz with 10-dB fractional bandwidth of 4.55%. The measured fractional bandwidth is slightly reduced from the desired 4.8% due to the fabrication errors. The two poles in the measured response are at 4.975 GHz and 5.12 GHz, while the intermediate frequency peak is at 5.03 GHz.

Fig. 2.5 shows the vector distribution of the E field at these three frequencies. The

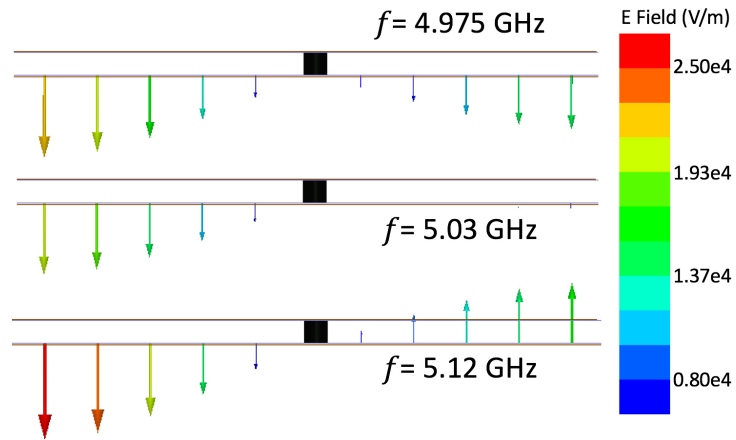


Figure 2.5: Simulated vector distribution of the electric field in the substrate on the cross section. Three frequencies refer to even mode, the mode at the intermediate peak frequency, and odd mode.

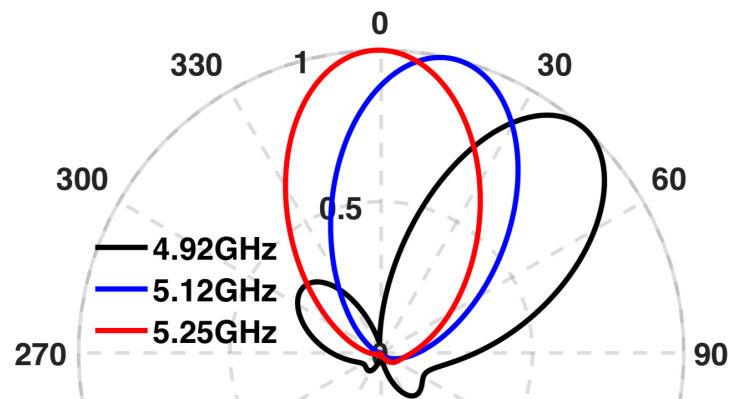


Figure 2.6: Simulated co-polarized radiation patterns on E plane. The patterns are normalized to 1 and shown in absolute value.

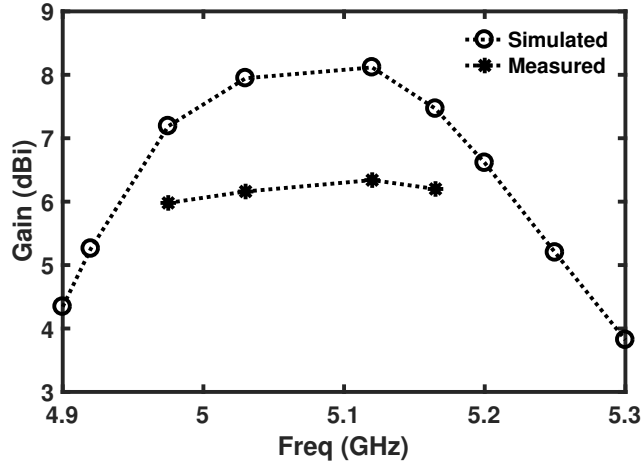


Figure 2.7: Realized boresight gain versus frequency. The measured gains, shown in this figure, are at 4.975 GHz, 5.03 GHz, 5.12 GHz, and 5.165 GHz respectively.

fields at 4.975 GHz and 5.12 GHz represent the even and odd mode field distributions respectively. The distributions are apparently asymmetric as designed. At 5.03 GHz, the fields at the two edges are around  $90^\circ$  out-of-phase. The field distributions for these three frequencies strongly support our theory that the phase difference at the two radiating slots changes with operating frequency.

To demonstrate the beam-steering capability of our design, we plot the simulated radiation patterns on E plane at three selected frequencies as shown in Fig. 2.6. The odd-mode frequency of 5.12 GHz is the frequency where maximum realized gain of 8.12 dBi is achieved in simulation. While at 4.92 GHz and 5.25 GHz, the realized boresight gain is 3 dB lower than the maximum one as shown in Fig. 2.7. The beam peak is at the broadside at 5.25 GHz, and it is at  $43^\circ$  at 4.92 GHz, which indicates a maximum  $43^\circ$  of scanning range within 3-dB gain band. The patterns are normalized to 1 and plotted in absolute values to provide a clear view of the beam steering.

The measured and simulated patterns on the E plane compare closely for even-mode, 90-out-of-phase, and odd-mode frequencies, as shown in Fig. 2.8. The peak of the co-polarized beam clearly scans from side to the center as the frequency changes. There is a -25-dB null at  $341^\circ$  on the co-polarized pattern at 4.975 GHz. This is the cancellation



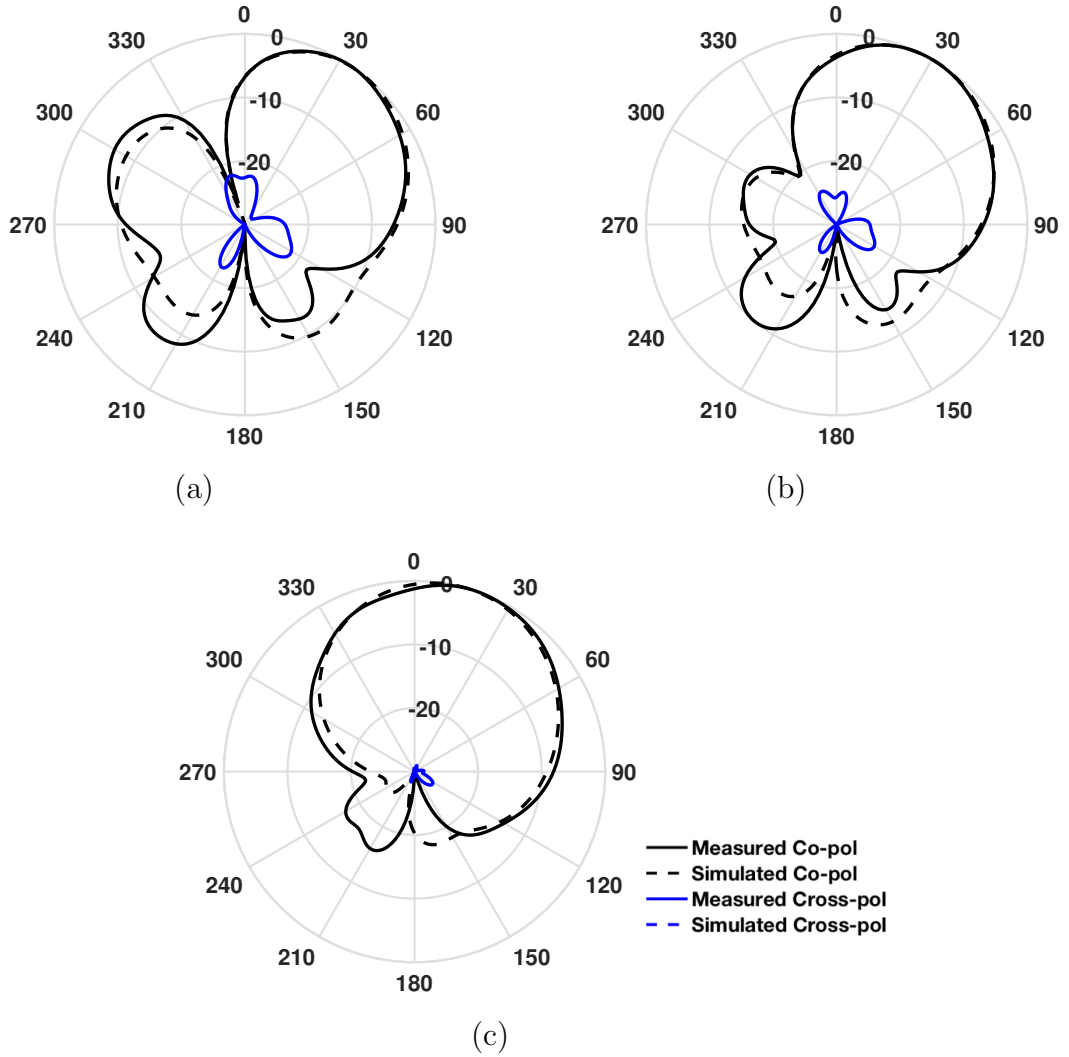


Figure 2.8: Simulated and measured radiation patterns on E plane at (a) 4.975 GHz (even mode), (b) 5.03 GHz (90° out of phase), and (c) 5.12 GHz (odd mode). The simulated cross-pol level is below the minimum scale -30 dB.

for the even-mode radiation as discussed above. The null scans to 324° as the frequency tuning to 5.03 GHz and disappears at 5.12 GHz. The measured cross-polarized patterns on E plane are all below -20 dB, though they are higher than the simulated ones due to fabrication and measurement tolerances.

The realized gain patterns at different frequencies on E plane are measured and shown in Fig. 2.9. The beam scans from 14° to 34° as the frequency changes from 5.165 GHz to 4.975 GHz. The maximum realized gain of 6.34 dBi is achieved at 5.12 GHz, the odd-mode

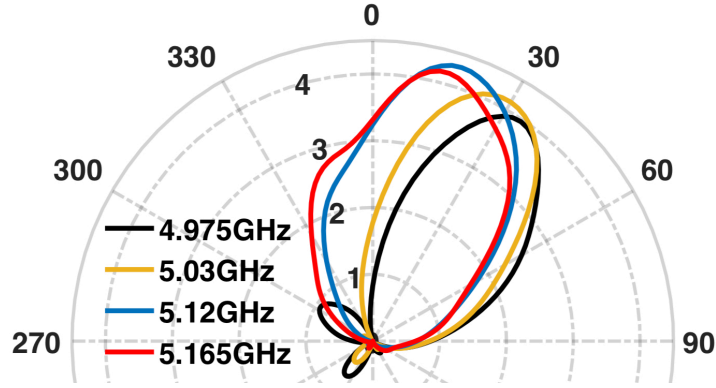


Figure 2.9: Measured realized gain patterns in absolute value on E plane.

frequency, as predicted by simulation. At even-mode frequency 4.975 GHz, the realized gain is 5.98 dBi with radiation efficiency of 70.1%. Radiation efficiency mentioned in this paper is the ratio of radiated power to input power, which does not account for reflection loss due to mismatch. The highest radiation efficiency within the matching band is 73.8% realized at 5.165 GHz, where the realized gain of 6.2 dBi is slightly lower than the maximum due to reflection loss.

As a comparison, a patch antenna, which has exactly same configuration as the proposed design but has no vias, is fabricated and measured. It matches at 5.03 GHz with 1.4% matching bandwidth. The measured realized gain is 6.85 dBi, and radiation efficiency is 78.2% at 5.03 GHz. In comparison to the regular patch antenna, the proposed antenna realizes the beam steering within a much wider matching bandwidth, and maintains similar radiation efficiency in the same time.

## 2.4 Conclusion

Coupled-mode patch antenna is presented. The design is implemented by putting vias to create two coupled half-mode cavities in a rectangular patch antenna. We are able to manipulate the phase difference between the two radiating slot and thus steer the beam through this design. Circuit model is built in order to control the coupling and achieve the wide matching bandwidth. The bandwidth can be further improved [8]. Measured and

simulated results show that the beam scans over a large range as the frequency changes while maintaining high radiation efficiency. The proposed beam-scanning antenna has advantages of compact size and low cost. More importantly, the proposed coupled-mode method opens the gate to realize different radiation features in compact antenna without compromise of size, cost, or robustness.

## CHAPTER 3

# Fixed-Frequency Wide-Range Beam Scanning CMPA

### 3.1 Introduction

The coupled-mode patch antenna (CMPA) realizes beam scanning without compromises of size, cost, or robustness [5], as discussed in Chapter 2. However, there are two main problems that prevent it from practical applications. The first issue is that CMPA steers beam as a function of frequency, while most communication systems operate at certain fixed frequency or band. Second problem is the relative narrow beam scanning range. The beam steering can only go from broadside to forward direction. It would be ideal if the beam scans in both forward and backward directions.

In this chapter, we present a fixed frequency beam steering CMPA controlled by one varactor diode loading to a slot on the ground. The loaded slot can equivalently become capacitive, resonant, or inductive as the capacitance of the varactor changes. It thus perturbs the cavity modes and field distributions which control the radiation beam in far

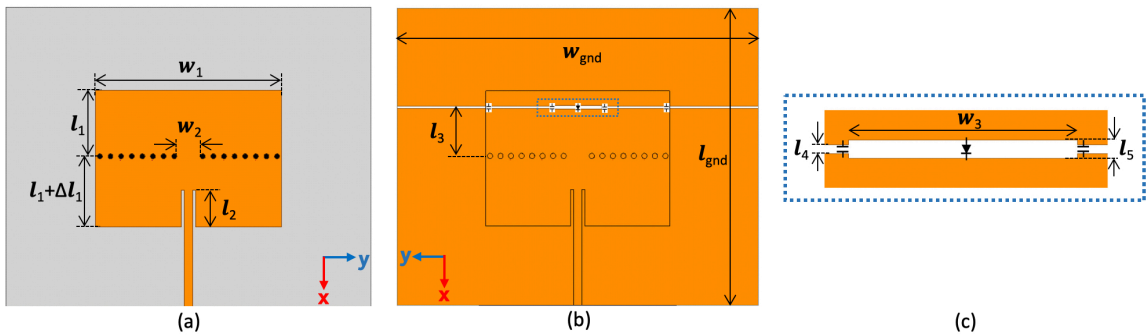


Figure 3.1: Schematic of the proposed antenna. (a) Top view. (b) Bottom view including the contour of the top patch. (c) Loaded slot.

field. In order to cover the whole tuning range, we mount two varactors with different tuning ranges, 9.24 pF-1.77 pF and 2.67 pF-0.63 pF, respectively at same location on the same antenna in fabrication. The measured and simulated frequency response and the beam steering are demonstrated, which show the objective forward and backward beam scanning through this single-element antenna tuned by a single varactor. The forward or backward radiation refer to the radiation whose beam peak is at positive or negative  $\theta$  region on E plane, respectively.

### 3.2 Antenna Design and Operation

Fig. 3.1 shows the schematic of the proposed antenna. The substrate is a ground-backed Rogers RT/Duroid 5880 substrate with dielectric constant of 2.2, loss tangent of 0.001, and height of 1.575 mm. As shown in Fig. 3.1 (a), the top is an inset-fed rectangular patch with width of  $w_1 = 56$  mm and inset feeding length of  $l_2 = 11$  mm. The metal shorting vias, represented by the black dots, divide the patch into two half-mode cavities with different lengths where  $l_1 = 19.75$  mm and  $\Delta l_1 = 1.5$  mm. A coupling gap with width of  $w_2 = 7$  mm is opened in the center of the via wall. The ground is  $w_{gnd} = 110$  mm by  $l_{gnd} = 90$  mm as shown in Fig. 3.1 (b). In order to easily apply bias, a slit is etched out of the ground that is  $l_3 = 14.75$  mm away from the via wall. The width of slit is  $l_4 = 0.6$  mm as shown in Fig. 3.1 (c). At the center of the slit, a slot with length of  $w_3 = 15$  mm and width of  $l_5 = 1.2$  mm is etched like a wider slit and loaded with a varactor diode. Four 10-pF capacitors are installed along the slit where two of them are nearby the slot and the other two are under the edges of the top patch. These capacitors compensate the inductive effect of the thin slit on the cavity mode within the operating band, and provide the DC block in the same time. On the other hand, the loaded slot does affect the cavity fields. The response of the proposed antenna can then be tuned by applying bias across the varactor.

A narrow transverse slot on microstrip line is equivalent to a series inductance since it concentrates the magnetic field locally [9]. The inductance value depends on not only the size of the slot but also the location, that is, where stronger the magnetic field is, bigger

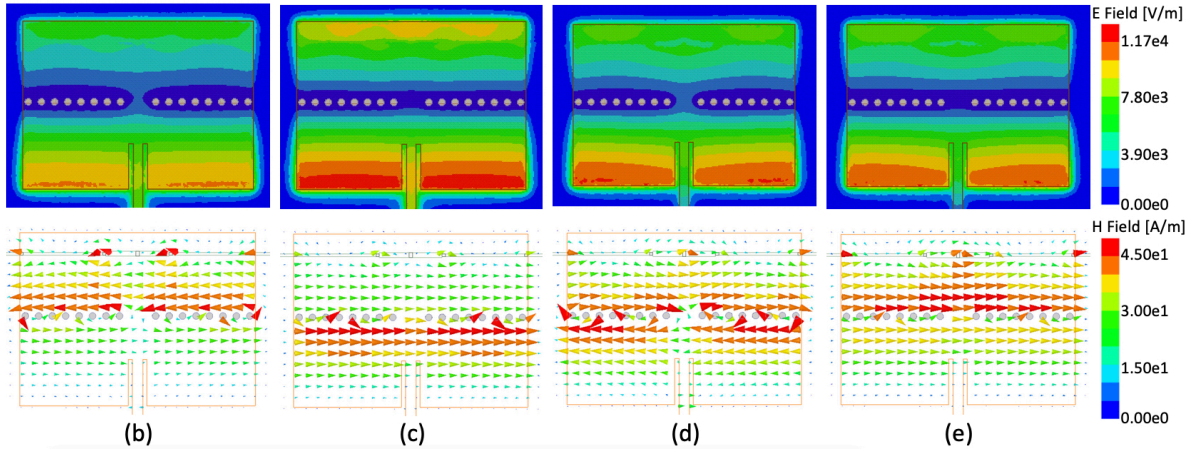
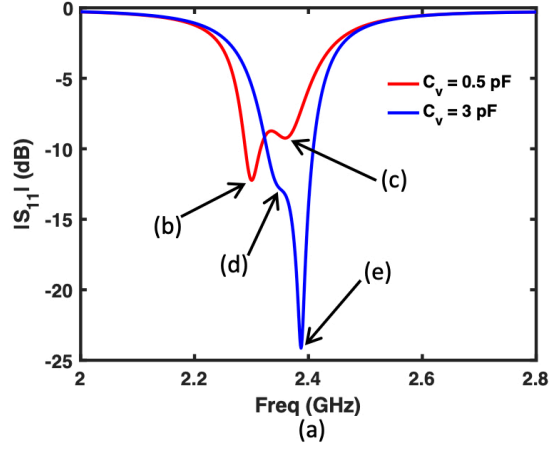


Figure 3.2: (a) Simulated frequency response of the antenna under different capacitances of the varactor  $C_v$ . The E and H field distributions in the cavity at (b) low frequency pole 2.301 GHz and (c) high frequency pole 2.363 GHz when  $C_v = 0.5$  pF; at (d) low frequency pole 2.348 GHz and (e) high frequency pole 2.387 GHz when  $C_v = 3$  pF. The varactor is simply modeled by a pure capacitor that is defined by RCL Boundary Condition in HFSS®.

the value can be. Loading the slot with a capacitor can make the whole configuration become capacitive, inductive, or resonant, depending on the equivalent inductance of the slot and the value of the capacitor. It has to be mentioned that the length of the slot  $w_3$  is much smaller than half wavelength and thus the slot itself is not an effective radiator. The effect of the slot is mainly on the guided fields in the cavity. In our antenna, we carefully design the slot and load it with a varactor to realize both capacitive and inductive response to the cavity within the varactor tuning range.

The varactor loaded slot, as part of the upper half mode cavity, affects the resonance of that cavity. Since the slot is serial to the major cavity mode, the resonant frequency of the cavity will be higher when the slot is capacitive than the one when the slot is inductive. On the other hand, the lower half mode cavity is not perturbed by the slot, and the upper and lower cavity will still be coupled through the open iris as long as the resonant frequencies of these two are close. Fig. 3.2 (a) shows the simulated frequency responses of the coupled two cavities when the loaded slot is inductive ( $C_v = 0.5$  pF) and capacitive ( $C_v = 3$  pF). The two-pole response in both cases proves the exist of the coupling. One of the poles overlays for both cases which indicates that the pole is corresponding to the resonance of the lower half mode cavity that is not affected by the slot. While the other pole shifts to high frequency as  $C_v$  changes from 0.5 pF to 3 pF, which indicates that the resonant frequency of the upper cavity increases since the loaded slot becomes capacitive.

The lower frequency poles for both cases in Fig. 3.2 (a) are corresponding to even mode. This is determined by the nature of magnetic coupling in the structure. The coupling effect increases the stored flux in each half mode cavity when the magnetic wall is inserted, and it decreases the stored flux when electric wall is in inserted [7]. In consequence, the frequency of even mode is always lower than the one of odd mode in our structure. To prove it, we plot the electric and magnetic field distributions at relevant frequencies with  $C_v = 0.5$  pF and  $C_v = 3$  pF in Fig. 3.2 (b-e). In both cases, the even and odd modes are excited. Shown in Fig. 3.2 (c) and (e), the E field at the coupling iris is zero, and the H fields of upper and lower cavities point to same direction at odd mode, because of the equivalent PEC wall. The opposite situations appear at even mode,

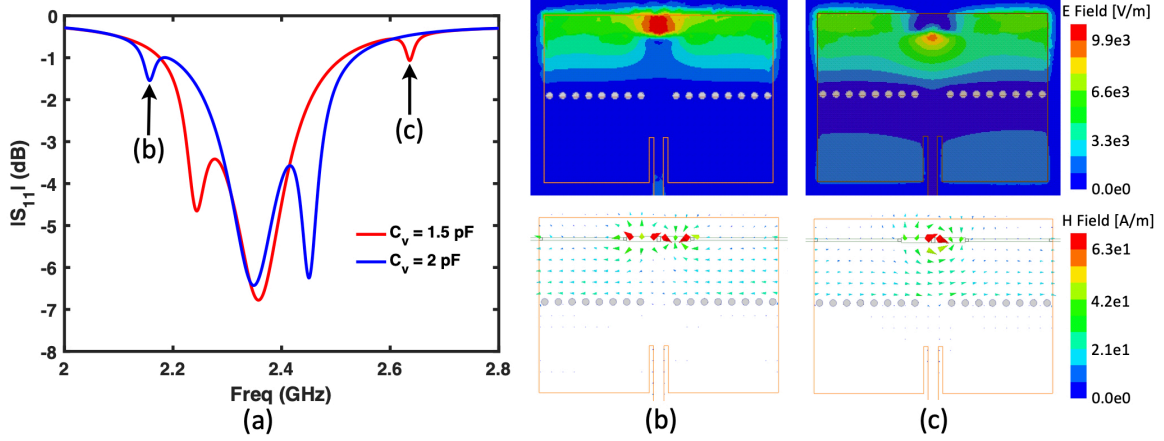


Figure 3.3: (a) Simulated frequency response perturbed by the slot resonance during the transition from capacitive to inductive. The poles pointed by black arrows are corresponding to the slot resonance, whose E and H field distributions at (b) 2.157 GHz when  $C_v = 2$  pF, and (c) 2.638 GHz when  $C_v = 1.5$  pF are plotted.

as shown in Fig. 3.2 (b) and (d), due to the PMC wall. Back to Fig. 3.2 (a), the odd mode (higher frequency pole) at  $C_v = 0.5$  pF overlays the even mode (lower frequency pole) at  $C_v = 3$  pF in certain frequency band. It means that at certain frequency, we are able to change the mode from even to odd by applying proper bias, and thus steer the beam in a wide angle range.

Due to the perturbation of the slot resonance, the frequency response of the antenna is not smoothly transferring while the loaded slot changes from capacitive to inductive, as shown in Fig. 3.3 (a). The additional pole corresponding to the slot resonance are pointed out by the black arrows. Since the equivalent inductance of the slot itself is basically fixed, the resonant frequency is highly dependent on the loading capacitance. The small leakage from the slot behaves like the load for the slot resonator, and results in the small poles shown in Fig. 3.3 (a). The resonant frequency of the loaded slot dramatically increases from 2.157 GHz to 2.638 GHz, when the loading capacitance  $C_v$  decreases from 2 pF to 1.5 pF in the simulation. When the resonant frequency of the loaded slot is around our operating frequency as the cases shown in Fig. 3.3 (a), the slot resonator will drain the income energy and disturb the fundamental coupling modes. Fig. 3.3 (b) and (c) illustrate



the E and H field distributions at the frequencies pointed in Fig. 3.3 (a) under the two different loading capacitances. The energy couples from the cavity and concentrates to the loaded slot, which interrupts the fundamental modes and cavity field distributions. Shown in Fig. 3.3 (b) E field distribution where  $C_v = 2$  pF, the fields are concentrated above the slot, while in (c) when  $C_v = 1.5$  pF, the fields are below the slot. This is because the weak coupling between the cavity and slot changes with the loading capacitance.

Based on the effect of the varactor loaded slot on the frequency response, the tuning can be sorted into capacitive range, resonant range, and inductive range. In capacitive and inductive range, the antenna has similar two-pole frequency response but in different bands. The pole that is corresponding to the resonance of upper cavity jumps to low frequency as the tuning changes from capacitive to inductive region as shown in Fig. 3.2 (a). Meanwhile, in either capacitive or inductive range, the frequency of the upper-cavity pole increases as the capacitance of the varactor decreases. This is because the varactor is serial to the cavity mode. In resonant range, on the other hand, an additional pole corresponding to the slot resonance appears, and the two-pole matching is disrupted. The gain of the beam, however, may not be perturbed much at some frequencies. We will discuss the relation of the frequency response and the radiation pattern, and demonstrate how the beam is steered by the bias voltage in next section.

### 3.3 Simulation and Measurement

Fig. 3.4 shows the views of the fabricated sample. The bias lines connect on the ground as shown in (a) and (b). Since the bias points are far from the resonant cavity, the high-frequency currents will not drain to the bias lines. In order to cover the whole tuning range, we use two types of plastic packaged varactors from Skyworks®), respectively in our sample, that is SMV1413 ranging from 9.24 pF to 1.77 pF and SMV1405 ranging from 2.76 pF to 0.63 pF. Keysight Advanced Design System (ADS®) and HFSS are used for hybrid simulation in this section to have precise varactor model and get accurate results. In our fabricated sample, the 10-pF capacitors are ATC 500 S Series Surface Mount Capacitors®), whose self resonant frequency is much higher than the operating

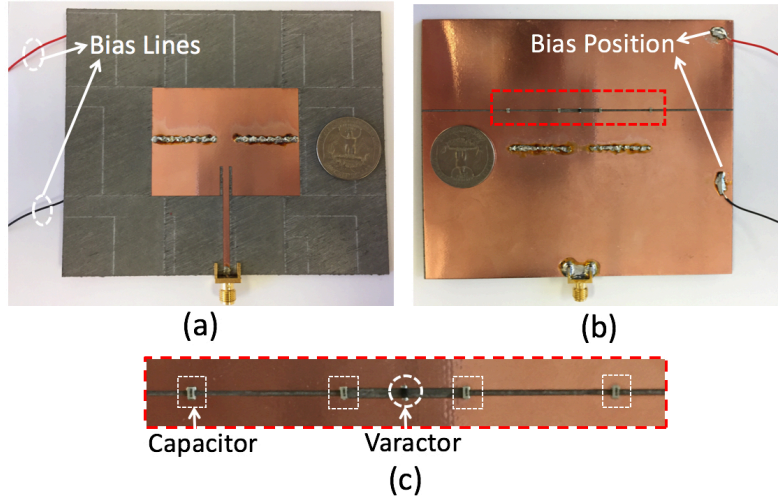


Figure 3.4: Fabricated sample of (a) top view, (b) bottom view, and (c) zoomed view for the loaded slot.

frequencies. They can then be treated as ideal capacitors in the simulation. The tuning is in capacitive range while using SMV1413, and it covers all three ranges while using SMV1405.

### 3.3.1 Performance with Varactor SMV1413

Our antenna is first loaded by Varactor SMV1413 that tunes the slot effective impedance to the cavity in the capacitive range. The simulated frequency responses under different capacitances are shown in Fig. 3.5 (a), where the equivalent circuit model of the varactor is given by the manufacturer. It can be seen that, when the capacitance decreases, the high-frequency pole, corresponding to odd mode, is moving to higher frequency while the low-frequency pole is basically not tuned. This is because the varactor loaded slot only affects the upper cavity and thus decreasing the capacitance will only increase the frequency of one pole as we discussed before. But it does affect the coupling since the discrepancy of the resonant frequencies for the two cavities becomes larger as the capacitance decreases. As a result, the matching is getting worse. Fig. 3.5 (b) shows the measured frequency responses under different bias voltages on the varactor. As the bias increases, the capacitance of the varactor decreases. Thus in Fig. 3.5, the measured plots (b) compare closely with the

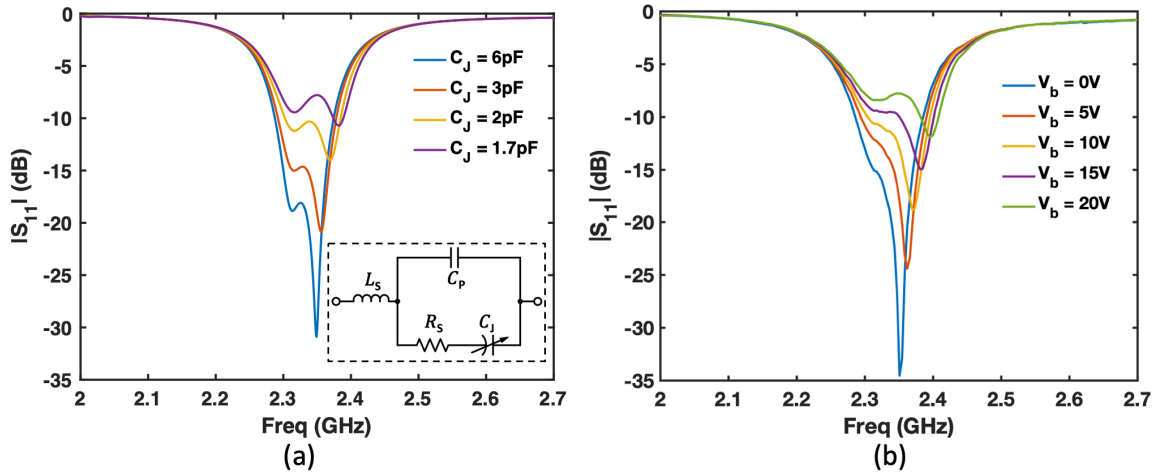


Figure 3.5: (a) Simulated frequency response under tuning of varactor SMV1413. The inset figure shows the equivalent circuit model of varactor, where the series inductance  $L_s = 0.7$  nH, series resistance  $R_s = 0.35\Omega$ , parallel capacitance  $C_p = 0.3$  pF, and junction capacitance  $C_J$  is tuned. (b) Measured frequency response under different bias voltages ( $V_b$ ) for varactor SMV1413

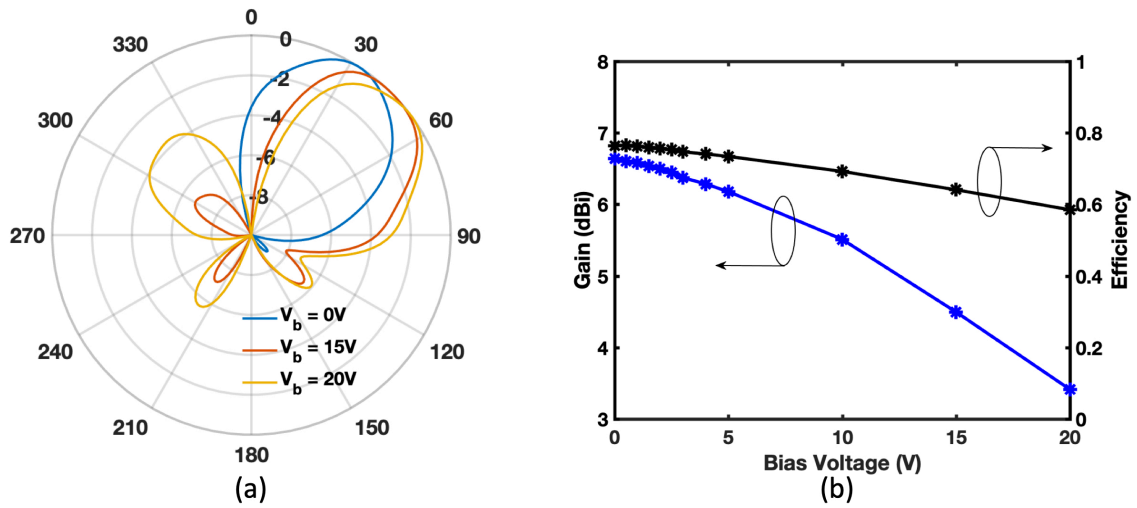


Figure 3.6: (a) Measured E-plane co-polarized radiation patterns under different bias at 2.35 GHz. The patterns are normalized and plotted in dB scale. (b) Measured peak gain and total efficiency of the antenna versus bias voltage at 2.35 GHz.

simulated ones (a) under the tolerance of the fabrication. The odd-mode pole shifts from 2.35 GHz to 2.40 GHz as the bias increases from 0 V to 20 V. Meanwhile, the even-mode pole remains at around 2.31 GHz.

At any fixed frequency around the high-frequency pole (odd mode), the phase of the radiating slots at backside (upper cavity) is changing as the pole shifting, and thus the beam scans. Fig. 3.6 (a) shows the measured patterns under different bias at 2.35 GHz, which is the frequency of the odd-mode pole for  $V_b = 0$  V. As the bias is tuned from 0 V to 20 V, the beam peak continuously scans from  $32^\circ$  to  $54^\circ$ . The measured peak gain and total efficiency versus bias voltage at 2.35 GHz are shown in Fig. 3.6 (b). The peak gain does not take the reflection loss into account, while the total efficiency does. The total efficiency at low bias voltages, where the matching is good, is around 76.5% which is comparable to that of a regular patch antenna with same size. This indicates that the loss caused by the varactor itself is relatively small. The peak gain decreases from 6.64 dBi to 4.20 dBi as the bias increases from 0 V to 20 V. This is because the mode at 2.35 GHz is odd mode when  $V_b = 0$  V where almost all energy radiates to the main beam direction. But it is getting close to even mode when the bias increases as shown in Fig. 3.5, which results in an additional side lobe at around  $\theta \simeq 50^\circ$  in the radiation pattern of  $V_b = 15, 20$  V as shown in Fig. 3.6 (a). Thus the energy radiated to the main beam direction decreases. In Fig. 3.6 (b), the total efficiency decreases as the bias voltage increases as well. The reason for that is because the matching is worse and the reflection loss increases.

The patterns have interesting behaviors under different bias at frequency around the low-frequency pole (even mode), though the pole itself does not shift much with the bias. Shown in Fig. 3.7 is the patterns for realized gain, which takes  $S_{11}$  into account, under different bias at the frequency of 2.3 GHz near the even-mode pole. Since the frequency is around the even mode, there are two beams respectively in positive (forward) and negative (backward)  $\theta$  region of the patterns. When bias  $V_b = 0$  V, the main beam is pointed at  $+60^\circ$  and most energy is radiated to the front side. This indicates the phase of the front radiation slot initially is delayed than the one of the back radiation slot. As

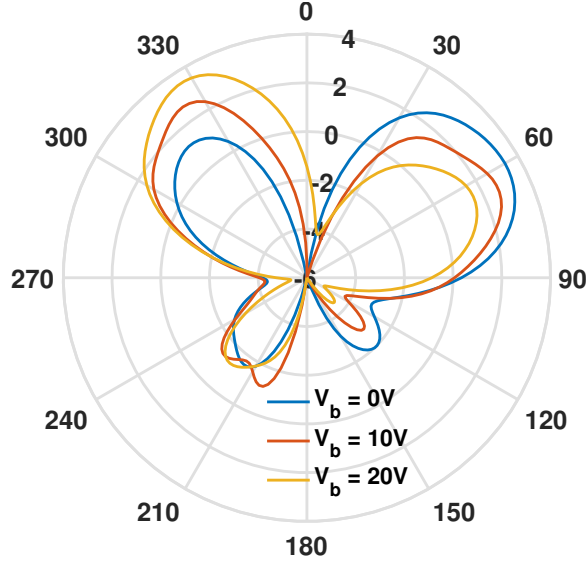


Figure 3.7: Measured co-polarized realized gain patterns under different bias at 2.3 GHz on E plane.

$V_b$  increases, the magnitude of the beam on the front side decreases while the one on the back side increases. When bias  $V_b = 20\text{ V}$ , the peak of the main beam turns to  $-32^\circ$  with basically same magnitude as the one at  $V_b = 0\text{ V}$ , which indicated the phase of the back slot is delayed than the front one. This is because when the capacitance of the varactor decreases, the loaded slot becomes more inductive that delays the field in the upper cavity, and thus gradually delays the phase at the back radiating slot. Since the slot will not affect the resonance in the lower cavity which means the front slot phase remains same, the relative phase of the back slot becomes delayed than the front one as the bias increases. This pattern behavior makes it possible for the beam of the antenna to scan from backward to forward as the bias changes.

### 3.3.2 Wide-Angle Scanning Realized by Varactor SMV1405

We then replace varactor SMV1413 with SMV1405 which has relatively low capacitance tuning range. The tuning ranges of the two varactors have overlays, and thus the slot loaded by SMV1405 is still in capacitive range when the bias is small. In Fig. 3.8, the measured  $S_{11}$  with SMV1413 under bias  $V_b = 10\text{ V}$  matches well with the one with SMV1405

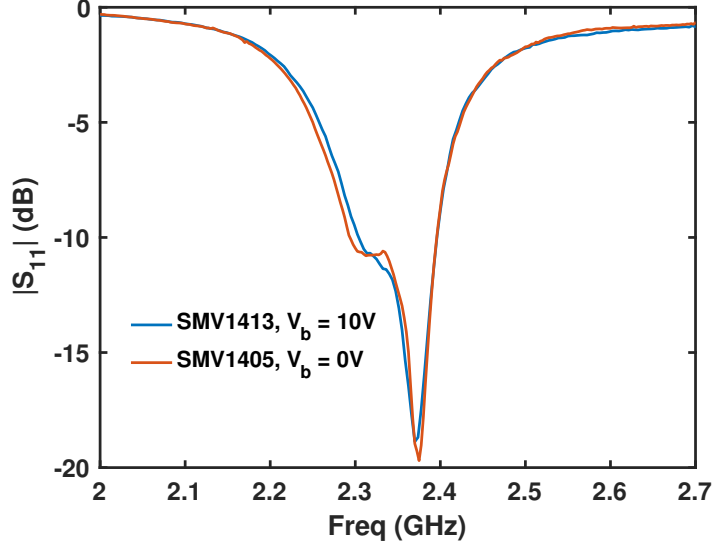


Figure 3.8: Comparison of the measured frequency response for the antenna loaded by two varactors respectively.

under bias  $V_b = 0$  V. This indicates that the transition from one varactor to the other is smooth, and the antenna loaded by SMV1405 under small bias will have similar response to the one discussed in previous subsection.

The varactor loaded slot becomes resonant around the operation frequency when the bias increases and the capacitance of the varactor further decreases. Simulated and measured frequency responses in the resonant range, shown in Fig. 3.9 (a) and (b) respectively, compare closely. Additional pole that is corresponding to the resonance of the loaded slot comes into the picture and interrupts coupling as we expected. Though matching is perturbed by the slot resonance, the pole corresponding to the resonance of the lower cavity remains at around 2.32 GHz. This is because the slot does not directly affect the resonance of the lower cavity or the external coupling between the feeding line and the lower cavity. The pole corresponding to the upper cavity shifts from right side to left side of lower cavity pole. As we discussed, the mode at lower cavity pole changes from even to odd mode consequently. When the bias keeps increasing, the additional pole gets to higher frequency and the loaded slot becomes inductive to the cavity.

Fig. 3.10 shows the measured frequency response to the bias. The transition from

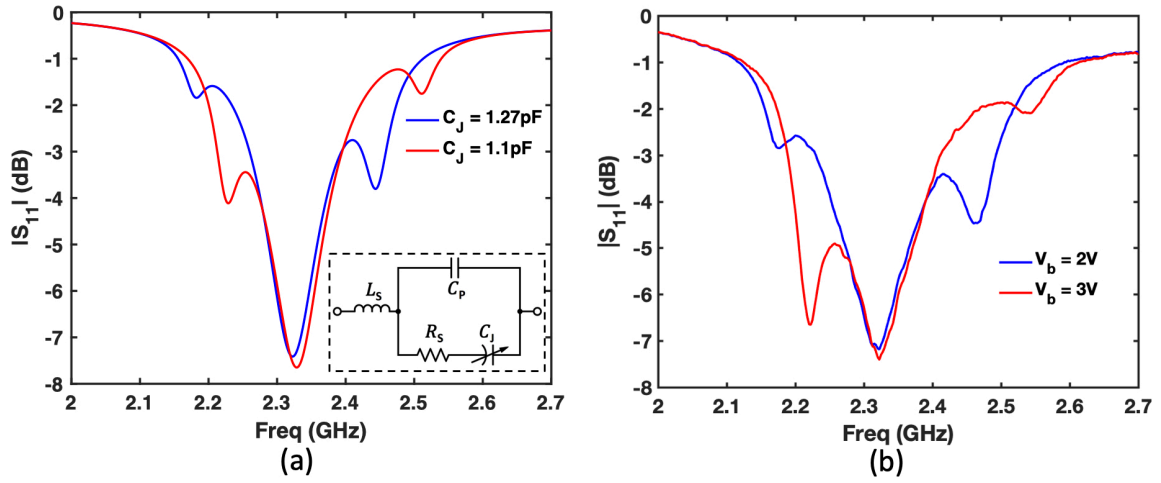


Figure 3.9: (a) Simulated frequency response under different junction capacitance in the resonant range. The values of the circuit model for SMV1405 are  $L_s = 0.7$  nH,  $R_s = 0.8\Omega$ , and  $C_p = 0.29$  pF. (b) Measured frequency response under different bias in the resonant range.

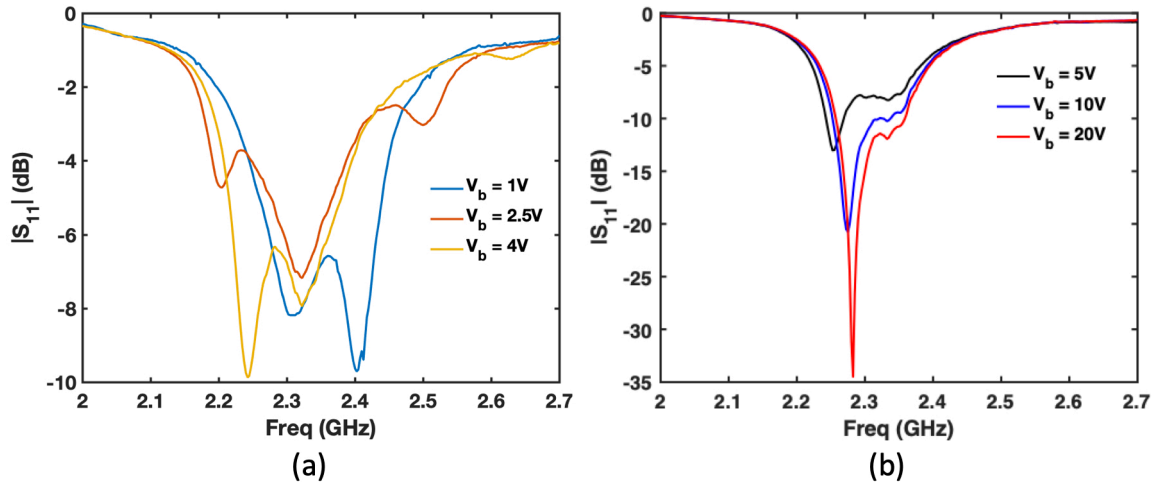


Figure 3.10: Measured frequency response under different bias in (a) the transition (resonant) range and (b) the inductive range.

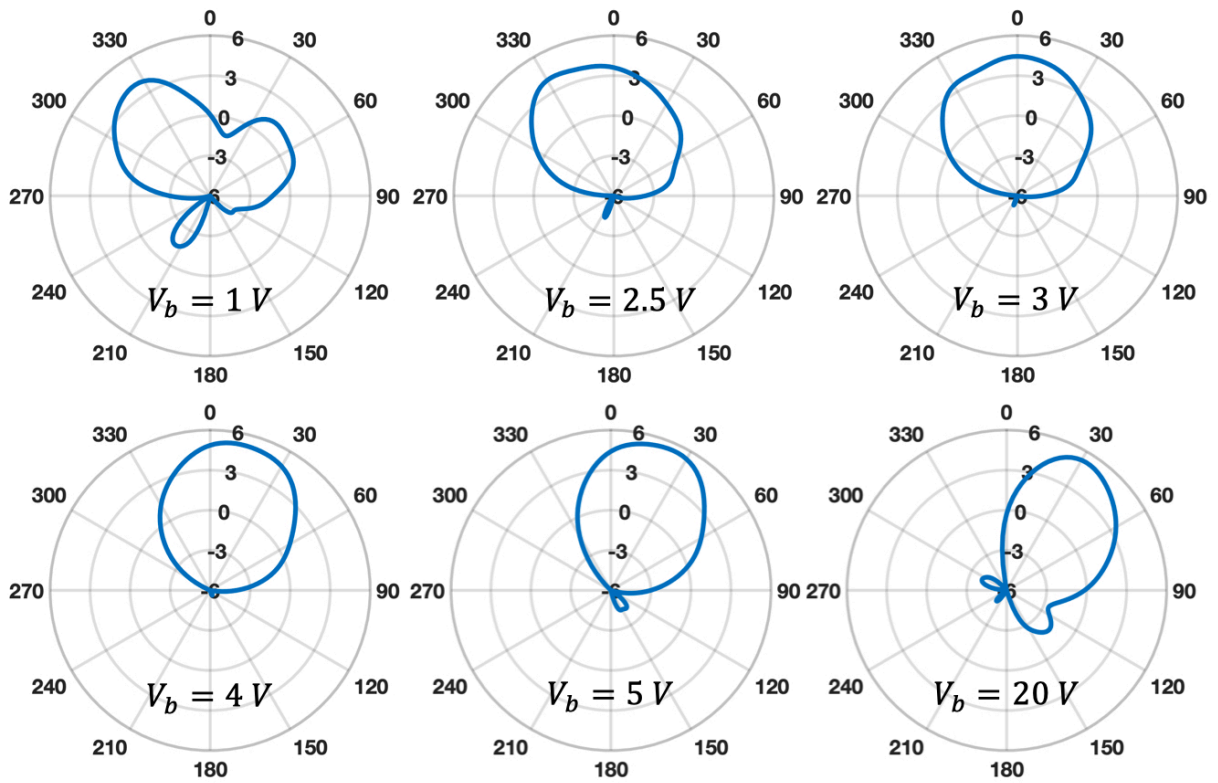


Figure 3.11: Measured co-polarized realized gain patterns on E plane under different bias at 2.29 GHz. The antenna is loaded with varactor SMV1405 only.



capacitive to inductive region is illustrated in Fig. 3.10 (a), where two-pole response at  $V_b = 1\text{V}$  first becomes three-pole due to the slot resonance, and then transfers back to two-pole response with frequency shifting to the left when  $V_b = 4\text{V}$ . Fig. 3.10 (b) shows the frequency response in the inductive range. The band of the two-pole response shifts to lower frequency compared to the response in capacitive range. The high-frequency pole, now corresponding to the resonance of the lower cavity, basically remains at same frequency. While the other pole corresponding to the upper cavity shifts to higher frequency as the bias increases and the loaded slot becomes more inductive. As the resonant frequencies of the two cavity come closer, the coupling becomes stronger and thus the band gets narrower and matching gets better. From the cavity field perspective, the phase on the back side slot gets delayed more as the bias increases. Consequently, at the frequency around the left-side pole, the radiation beam of the antenna scans with the bias. Meanwhile at around 2.3 GHz, the frequency response in capacitive, resonant, and inductive ranges overlay, where the maximum beam scanning range can be realized.

Fig. 3.11 presents the measured realized gain patterns of the antenna at 2.29 GHz under different bias. As the bias voltage increases, the main beam of the antenna continuously scans from backward to forward. The beam points to broadside at bias  $V_b = 3\text{V}$ . The peak of the beam scans from  $-34^\circ$  to  $+32^\circ$  as the bias increases from 1 V to 20 V, which results in a total scanning range of  $66^\circ$ . The realized peak gains under different bias are all above 4 dBi. The whole tuning is realized by only one varactor, SMV1405 model.

The corresponding peak gain and total efficiency are measured under different bias as shown in Fig. 3.12. Again, the peak gain does not account for the reflection loss while the total efficiency does. At  $V_b = 1\text{V}$ , the loaded slot is still capacitive and the beam shares similar pattern to the one discussed in Fig. 3.7. So the peak gain of 4.91 dBi is relatively low due to the side lobe of the even mode, but the total efficiency of 68.2% is high since the matching is still good. As the bias increases to 4 V, the gain increases to maximum of 6.27 dBi while the total efficiency drops to minimum of 58.5%. This is because the mode at 2.29 GHz switches from even to odd and thus the side lobe gradually disappears which leads to the higher gain; on the other hand, the matching is much perturbed by

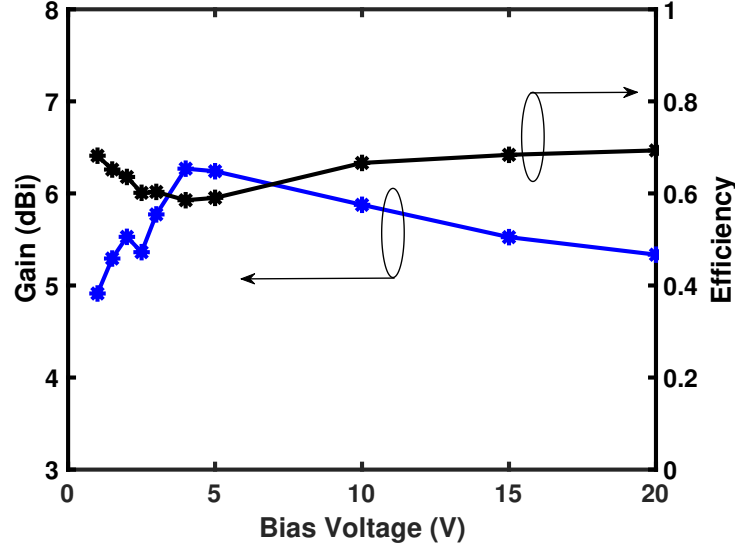


Figure 3.12: Measured peak gain and total efficiency of the antenna versus bias voltage at 2.29 GHz.

the slot resonance and thus the reflection loss increases which leads to the decrease of total efficiency. As  $V_b$  increases from 5 V to 20 V, the total efficiency gradually increases to 69.3% due to better matching as shown in Fig. 3.10 (b). In the meantime, the even mode pole modes toward 2.29 GHz, and thus the side lobe appears as shown at  $V_b = 20$  V in Fig. 3.11. The peak gain then slightly decreases to 5.33 dBi at  $V_b = 20$  V. In general, the peak gain and total efficiency within the whole tuning range shown in Fig. 3.12 is comparable to the ones of a regular patch antenna with same size and substrate.

### 3.4 Conclusion

A single-element beam scanning antenna controlled by only one varactor is presented. The design is based on coupled-mode patch antenna whose operation is explained by the coupled even and odd modes and two-element array factor. A varactor loaded slot etched on the ground of one of the half-mode cavities is tuned to be capacitive, resonant, or inductive. Two types of varactors, SMV1413 and SMV1405, have been used to cover the whole tuning range. The phases of the radiating slots are then manipulated by applying

bias, which leads to both forward and backward beam scanning. Maximum scanning range of  $66^\circ$  is achieved at 2.29 GHz where the beam continuously scans from  $-34^\circ$  to  $+32^\circ$ . The gain and efficiency of this design is comparable to the ones of a regular patch antenna with same size and substrate.

The design is reliable and robust since all the tuning is simply realized by one component. It has the advantages of compact size, simple and low-loss operation, wide range of continuous beam scanning, low cost, and friendly fabrication. The design can be scaled to different frequency domains, and therefore find its applications in many scenarios.

## CHAPTER 4

### Endfire CMPA with Vertical Polarization

#### 4.1 Introduction

Endfire antennas with polarization perpendicular to the ground, also known as vertical polarization, are desired in many modern communications. The endfire pattern offers strong radiations on the horizontal plane which is preferred for the communications between systems on a horizontal platform, like ground-wave or vehicle-to-vehicle communication. In the meantime, the wave with vertical polarization, compared to that with horizontal polarization, suffers less attenuation and less disruption on the polarization during propagating along the ground. Traditional Yagi-Uda antenna [10] assembled to be perpendicular to the ground, as an example, has been widely used due to its high directivity. The antenna is typically implemented by a set of metal wires as an array of electric dipoles. It, thus, suffers from the heavy and bulky structure.

Planar microstrip Yagi array antennas [11–14], which integrate the Yagi arrays onto low profile substrate by using microstrip-type radiators, have been reported. These antennas benefit from the low profile, friendly fabrication, and high directivity. However, the radiations of those designs are either horizontally polarized, or are pointed away from endfire direction, which will waste more input energy to maintain the same endfire communication. In addition to Yagi-Uda antenna, dominant mode leaky-wave antenna [2] has been claimed to have the capability of endfire radiation. The idea is to control the propagation constant of the leaky wave. But, its peak gain, again, is away from endfire direction.

Besides the Yagi antennas, low-profile Vivaldi antennas, or tapered slot antennas, are capable to radiate endfire beams [15–17]. This type of antenna applies tapered slot,

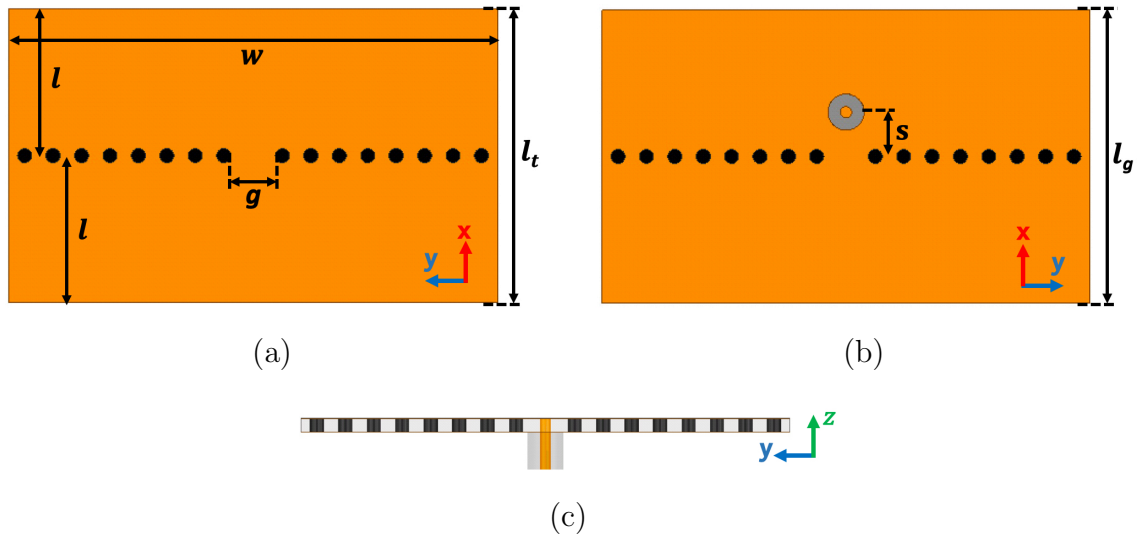


Figure 4.1: Schematic of the proposed design. (a) Top view. The black dots represent the metal via posts, with diameter of 1.6 mm and spacing of 3.2 mm, connecting top patch to the ground. The dimensions are all in mm:  $l = 16.5$ ,  $l_t = 33$ ,  $w = 55$ ,  $g = 5$ . (b) Bottom view. The ground metal and the substrate have same size as the top patch,  $l_g = l_t$ . The gray hole is the etched out of the ground for the feeding coaxial waveguide, whose inner diameter is 1.27 mm and outer diameter is 4.1 mm. The center of the feeding is located at  $s = 5$  mm. (c) Back view. The antenna is back-fed from bottom.

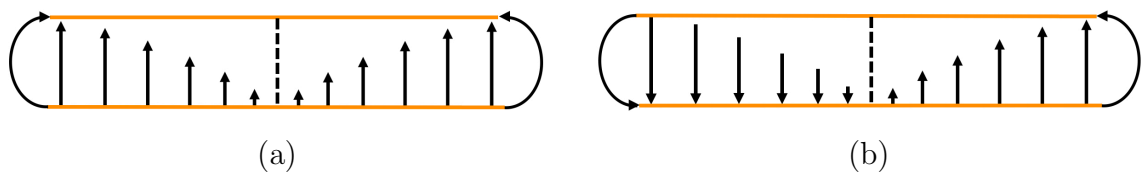


Figure 4.2: The demonstration of the E field vector distribution in the coupled cavity for (a) even mode and (b) odd mode.

which typically is integrated onto thin substrate, to radiate energy out. The biggest advantage of Vivaldi antennas is their broadband response, which makes them very useful for ultrawide-band (UWB) applications. Due to the radiation mechanism, those antennas are fundamentally limited to the horizontal polarization.

In this chapter, the concept of CMPA [5, 18] is applied to realize endfire radiation with vertical polarization. The length of the proposed antenna is designed to be around quarter wavelength which enables its endfire patterns. The coupling modes are excited inside the cavity similar as CMPA. The back-fed coaxial feeding brings additional phase shift to the edge fields at one side, which makes the beam of this antenna pointing to the forward endfire,  $\theta = 90^\circ$ , at both even and odd mode. The ground is designed to be the same size as the top patch which further reduces the antenna size and avoid undesired diffraction of the ground edges. In this way, the radiation of the antenna points to endfire exactly which is proved by the simulated results. During the measurement, however, the antenna, like dipole antenna, suffers from the unbalanced current, also known as common mode current, carried on the outside of feeding coaxial cable. The undesired current radiates and perturbs the antenna patterns. So a quarter wavelength sleeve (bazooka) balun is designed as the common mode choke outside the feeding coaxial feeding. The measurement shows good  $S_{11}$ , realized endfire gain, front-to-back (F/B) ratio, and total efficiency as expected. The simulated and measured patterns of the sample on Elevation ( $xz$ ) and Azimuth ( $xy$ ) plane compare closely and demonstrate the endfire radiation of the design.

## 4.2 Design and Operation

The schematic of the proposed antenna is shown in Fig. 4.1. The size of the antenna is characterized by the width  $w$ , top patch length  $l_t = 2l$ , and ground length  $l_g = l_t$ . A ground-backed Rogers RO4350B with dielectric constant of 3.66 is chosen to be the substrate so that the length of the antenna is roughly equal to quarter wavelength in free space,  $l_t = l_g \simeq \lambda_0/4$ . It has loss tangent of 0.0031, and height  $h = 1.524$  mm. As a model of actual SMA connector, a coaxial waveguide, with inner diameter of 1.27 mm and outer

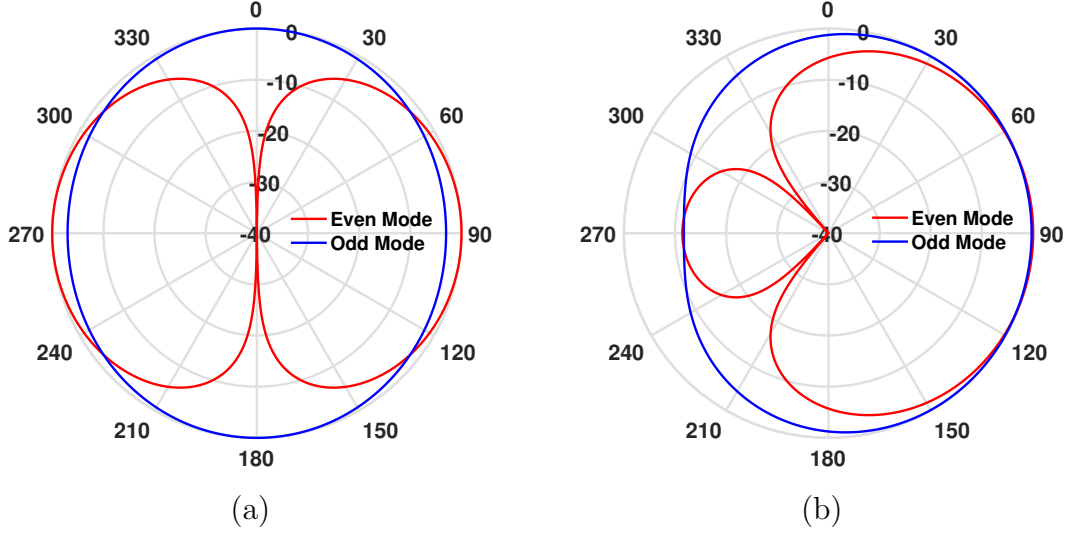


Figure 4.3: Pattern of even and odd mode calculated by Eq. (4.1) with additional phase shift of (a)  $\phi_1 = 0^\circ$  and (b)  $\phi_1 = 60^\circ$ .

diameter of 4.1 mm, is back-fed to the antenna. A row of metal via posts connecting top patch to the ground is put at the center with a gap of 5 mm in the middle as coupling iris. So the whole cavity, similar to CMPA, will support even and odd mode as two eigenmodes as shown in Fig 4.2. The radiating fringing fields at the edges indicate that the polarization is perpendicular to the ground (vertical polarization).

#### 4.2.1 Model of Two-Element Array

The radiation of the antenna is contributed by two equivalent magnetic currents at the radiating slots. In a completely symmetric model, those currents with same magnitude are  $180^\circ$  out-of-phase at even mode and in-phase at odd mode [5]. The pattern of the antenna on E plane is thus dependent on array factor of two elements

$$AF = 2 \cos \left[ \frac{1}{2} (k_0 d \sin \theta + \Delta\phi) \right] \quad (4.1)$$

where  $k_0$  is the propagation constant in free space;  $d$  is the separation distance; and  $\Delta\phi$  is the phase difference of the two currents. For simplicity, let us assume each of the magnetic currents radiates omnidirectionally on E plane.

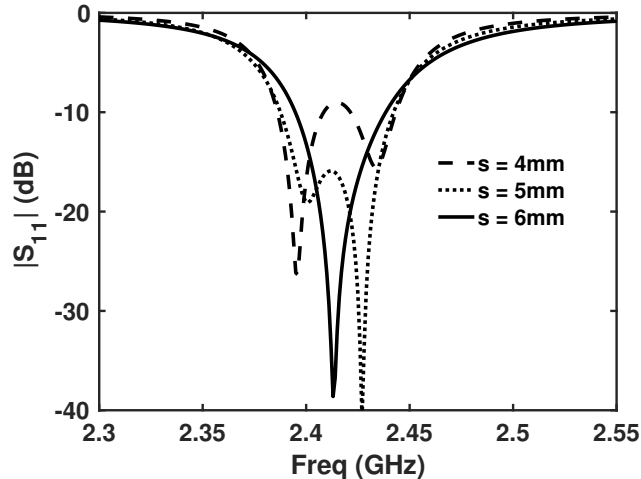


Figure 4.4: Simulated frequency responses of the antenna with different excitation locations, where  $s$  is the distance between the center via wall and the feeding pin as shown in Fig. 4.1.

If the separation distance is quarter wavelength, then at even mode  $\Delta\phi = 180^\circ$ , the antenna has symmetric backward  $\theta = -90^\circ$  and forward  $\theta = 90^\circ$  endfire beams; while at odd mode  $\Delta\phi = 180^\circ$ , it has symmetric upward  $\theta = 0^\circ$  and downward  $\theta = 180^\circ$  broadside beams as shown in Fig. 4.3 (a). Though the even mode offers the endfire radiation, the pattern dramatically changes as the frequency changes from even to odd mode. As an endfire antenna, the desired design should be able to radiate most energy towards one endfire direction, either backward or forward, within the whole matching band.

The solution is to bring in additional phase shift  $\phi_1$  to one of the elements. If there is such additional phase shift, the phase difference at even mode is  $\Delta\phi = \pm 180^\circ + \phi_1$  and it is  $\Delta\phi = -\phi_1$  at odd mode, due to the boundary condition for the two eigenmodes. With properly selected  $\phi_1$ , the beam at forward endfire will be larger than one at backward for even mode; while for odd mode, the two beams, which originally point upward and downward, will approach to forward endfire. The normalized patterns of AF for even and odd mode with  $\phi_1 = 60^\circ$ , calculated from Eq. (4.1), are plotted in Fig. 4.3 (b) to illustrate this idea. With the additional phase shift, the beams for both modes point to forward endfire despite of the slight changing of the patterns. As predicted by Eq. (4.1),



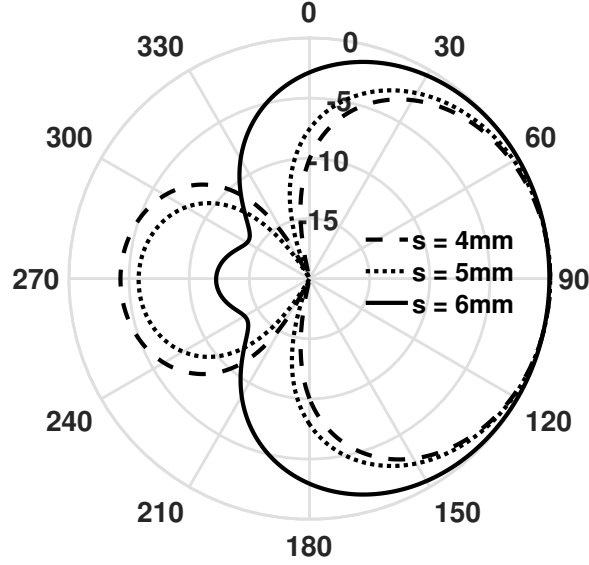
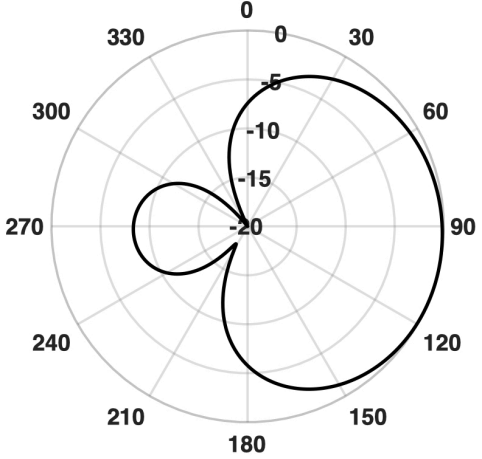
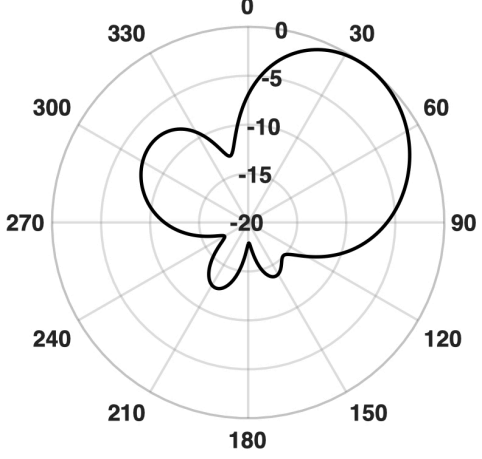
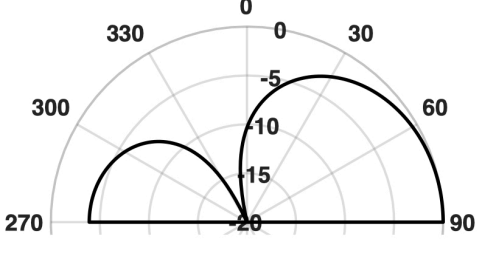


Figure 4.5: Simulated radiation patterns of the antenna with different excitation locations at even-mode pole on  $xz$  plane of cut.

the directivity of odd mode is not maximum at exactly forward endfire, but it is very close to the maximum as shown in Fig. 4.3 (b).

In our design, the feeding breaks the symmetry of the excited cavity modes, and results in the phase shift. To prove that, we sweep the feeding location in the simulation, and plot the frequency responses in Fig. 4.4. Fig. 4.4 illustrates that the feeding location affects the resonant frequencies of the excited modes. To be more specific, as the feeding moves away from the center, the two frequency poles move closer to each other. This indicates that the location of the excitation has an impact on the coupling, and thus on the excited coupled modes. To further demonstrate the impact on the phase shift, we track the even-mode pole (low frequency pole) and plot the simulated radiation patterns in Fig. 4.5. As shown in Fig. 4.5, when the excitation moves away from the center, the  $-x$ -direction side lobe becomes smaller, which indicates more phase shift. In other words, the excitation/feeding causes more phase shift when it is more asymmetrically located (away from center). As a conclusion of Fig. 4.4 and 4.5, there is a trade-off between the phase shift and the matching bandwidth in a sense. The feeding location of our antenna is designed to balance that. It has to be mentioned that in the simulations discussed in this

Table 4.1: Ground plane effect on the main lobe direction of the proposed antenna

Ground Length	Radiation Pattern of Even Mode
$l_g = l_t$	 <p>A polar plot showing the radiation pattern for <math>l_g = l_t</math>. The plot is on a circular grid with radial lines every 30 degrees from 0 to 330 and concentric circles representing dB levels from 0 to -20. The main lobe is directed towards 90 degrees, reaching approximately -5 dB. A secondary lobe is visible at 270 degrees, reaching approximately -15 dB. The pattern is roughly heart-shaped, pointing towards the right.</p>
$l_g = 4l_t$	 <p>A polar plot showing the radiation pattern for <math>l_g = 4l_t</math>. The grid is the same as the first plot. The main lobe is still directed towards 90 degrees but is significantly narrower and deeper, reaching approximately -10 dB. A secondary lobe is now directed towards 270 degrees, reaching approximately -15 dB. The pattern is more complex and narrower than the first case.</p>
$l_g = \text{inf}$	 <p>A polar plot showing the radiation pattern for <math>l_g = \text{inf}</math>. The grid is the same. The radiation pattern is now a simple semi-circle centered at 0 and 180 degrees, extending from 90 to 270 degrees. The main lobe is at 90 degrees, reaching approximately -5 dB, and the pattern is symmetric about the 180-degree axis.</p>

paragraph, the ground hole is removed to eliminate its effect when sweeping the feeding location, and the antenna is excited by the embedded feeding pin, instead of the outside coaxial waveguide.

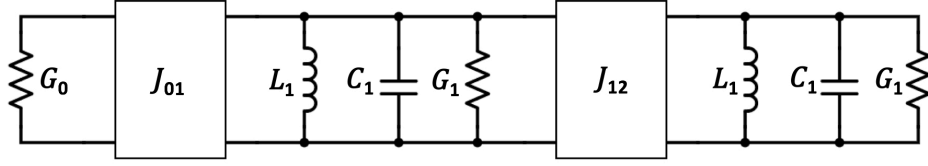


Figure 4.6: Equivalent lumped circuit model of the proposed antenna, where  $G_0 = 0.02 S$  stands for source,  $J_{01} = 1.23 \times 10^{-3} S$  for external coupling,  $J_{12} = 3.6 \times 10^{-4} S$  for internal coupling,  $L_1 = 0.45 \text{ nH}$  and  $C_1 = 9.67 \text{ pF}$  for each of the half cavities, and  $G_1 = 2.17 \times 10^{-3} S$  for the radiation loss.

#### 4.2.2 Finite Ground Plane Effect

The reason why many endfire antenna designs like [14] cannot get the beam exactly point at endfire is because of the effect of the finite ground plane. It has been reported by J. Huang in [19] how the finite ground plane affects the radiation pattern of a rectangular patch antenna. Huang compared the patterns calculated by geometrical optics (GO) with those by geometrical theory of diffraction (GTD), and concluded that the diffraction of the ground edge plays an important role of the broadside pattern of a microstrip patch antenna. The effect of the finite ground is even more important for the endfire antennas. GTD can certainly be applied here to find the effect, but nowadays it is more convenient to calculate the patterns with modern full-wave simulators.

The proposed antenna is simulated at even mode with different ground length  $l_g = l_t, 4l_t, \text{inf}$  and the radiation patterns on E-plane are compared in Table 4.1. All three patterns point forward in the  $+x$  half plane because of the additional phase shift as discussed before. If there is no ground effect, the patterns should not change much since the antenna is always operating at even mode. However, the main beam of the finite ground  $l_g = 4l_t$  points to  $\theta = 38^\circ$  while the beams for the other two cases are to forward endfire  $\theta = 90^\circ$ . It indicates that a finite ground, larger than the top patch, reflects the beam more to the upside which makes the endfire radiation hard to be achieved. While

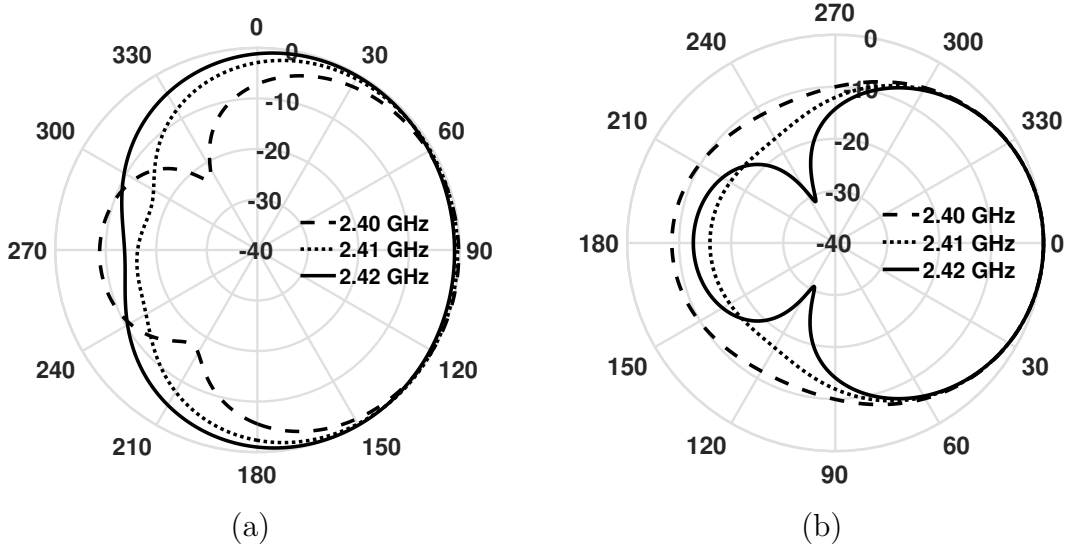


Figure 4.7: Simulated co-polarized normalized patterns of the antenna on (a) Elevation ( $xz$ ) plane and (b) Azimuth ( $xy$ ) plane for different frequencies. The direction angles are  $\theta$  in (a) and  $\phi$  in (b).

in the case of  $l_g = l_t$ , the fringing fields directly radiate to the free space without any ground reflection, and thus the beam is exactly at endfire as predicted by Eq. (4.1).

In practice, mounting the antenna on a much larger ground in terms of wavelength, which behaves like an infinite ground, will solve the problem. Another approach is taken for the proposed design, that is, truncating the ground to have the same size of the top patch which offers the endfire radiation as well. In the meantime, the overall size of the antenna itself is reduced, though it comes with a price of lower gain compared to that of infinite ground. The design, of course, can be mounted to any ground-like platform if necessary, which then will have the pattern similar to that of  $l_g = 4l_t$  or  $l_g = \text{inf}$  depending on the size of the platform.

### 4.2.3 Circuit Model

In Fig. 4.6, the equivalent circuit model of the antenna is developed with the method mentioned in [7]. Similar to CMPA [5], the model has only one port as source but no load port. The input energy of the antenna radiates to the free space through the two radiating slots. Due to the symmetry of the design, the same radiation conductance  $G_1$  is

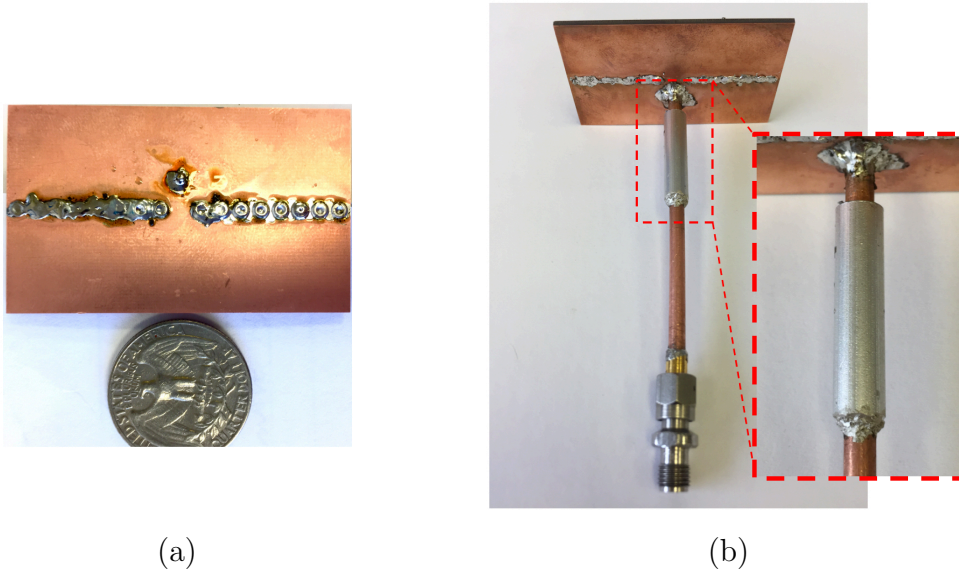


Figure 4.8: The fabricated antenna fed via a quarter-wavelength bazooka balun from (a) top view and (b) side view with the balun zoomed in.

used for both of two half-mode cavities, which is equivalent to the load port in the circuit model. For same reason, the same shunt LC circuits is built to represent the resonance of each half-mode cavity. The circuit model offers a deep understanding of the frequency response which guides the optimization of our design.

### 4.3 Simulation and Measurement

Fig. 4.7 shows the simulated co-polarized patterns of the propose antenna itself on Elevation plane (E plane,  $xz$  plane) and Azimuth plane ( $xy$  plane). The patterns are plotted at the frequencies corresponding to the even and odd modes and at the center frequency. At even and odd mode frequencies, the patterns on Elevation plane are very close to the ones calculated by Eq. (4.1) as shown in Fig. 4.3 (b). It also indicates that the undesired ground effect for our design is negligible as expected. The main beams of all frequencies point to forward endfire direction despite of the slight pattern changing. The F/B ratio is around 16 dB at 2.41 GHz, higher than those at the other two frequencies. This is because the phase difference  $\Delta\phi$  is closer to  $90^\circ$  at the intermediate frequency as indicated by Eq. (4.1). During the measurement, however, we notice that the patterns for this endfire

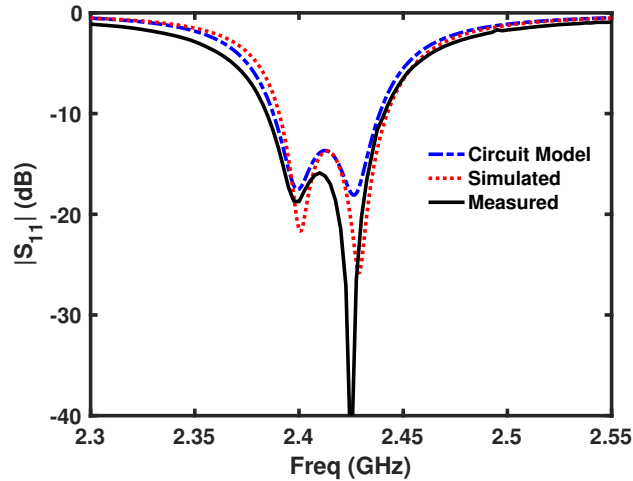


Figure 4.9: The simulated and measured  $S_{11}$  response for the antenna with balun. The measured result of the antenna without balun is also plotted as a reference.

antenna is perturbed by the undesired radiation from the unbalanced current carried on the outside of the coaxial cable. As a result, a common mode choke is required for the implementation.

Fig. 4.8 shows the fabricated sample fed via a quarter-wavelength sleeve (bazooka) balun. The balun serves as a common mode current choke which blocks the current carried on the outside of the coaxial cable and thus avoids the energy waste and undesired radiations. The reflection coefficient is measured by Agilent 8510C Vector Network Analyzer. Shown in Fig. 4.9, the circuit-model, simulated, and measured  $S_{11}$  responses match well with each other. The measured 10-dB bandwidth for the new sample is 2.5% with center at 2.41 GHz, which is doubled compared with the bandwidth of a regular patch antenna with same size and substrate. The slight discrepancy between the measurement and simulation is due to the fabrication tolerance. High selective two-pole frequency response is achieved as expected, where the even mode and odd mode are measured at 2.40 GHz and 2.425 GHz respectively.

The simulated and measured patterns of the sample fed via balun are plotted in Fig. 4.10. The measured co-polarized patterns on both planes match well with the simulated ones, which together show the endfire radiation of the proposed antenna with the

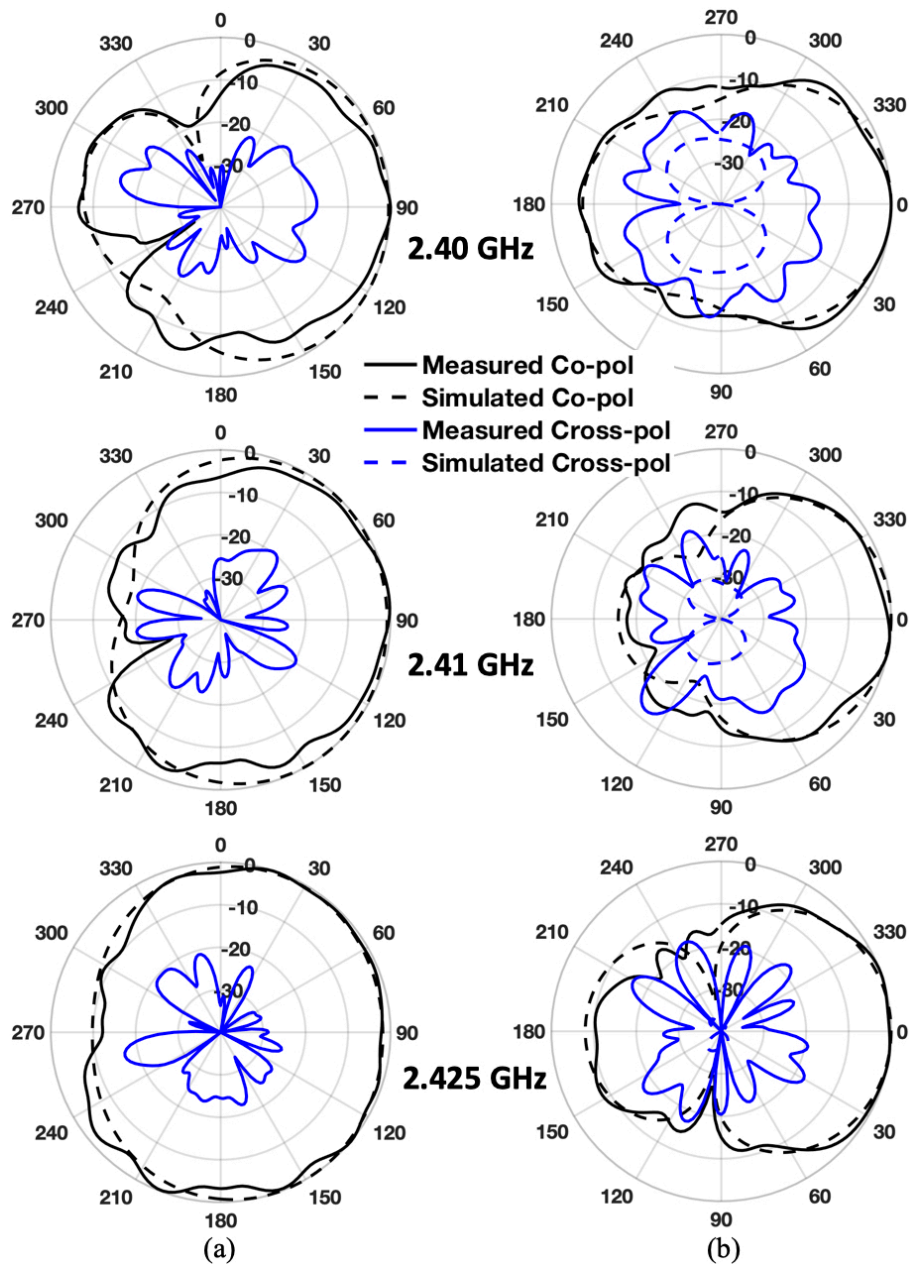


Figure 4.10: Measured and simulated normalized patterns for the antenna with balun on (a) Elevation ( $xz$ ) plane and (b) Azimuth ( $xy$ ) plane at even mode 2.40 GHz, intermediate frequency 2.41 GHz, and odd mode 2.425 GHz.

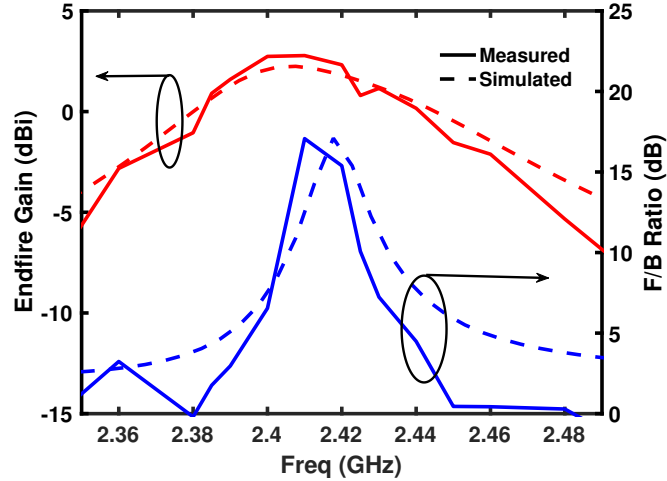


Figure 4.11: Measured and simulated forward endfire realized gain and F/B ratio versus frequency.

beam peak pointing at forward endfire direction. The measured cross-polarized patterns are below -15 dB in general, though they are higher than the simulated ones due to fabrication and measurement tolerances.

Fig. 4.11 shows the forward endfire realized gain and F/B ratio of the proposed antenna. The measured and simulated results compare closely. The measured 3-dB bandwidth of realized gain at forward endfire direction is 2.5% with maximum gain of 2.8 dBi at center frequency of 2.41 GHz. Considering the compact size of this antenna, the endfire realized gain is actually good. At center frequency, the measured front-to-back (F/B) ratio has a maximum value of 17.1 dB which indicates the good performance of the endfire radiation. The F/B ratio becomes close to 0 dB as the frequency moves away from the center. This is because as the frequency moving away, the phase difference  $\Delta\phi$  is getting close to  $0^\circ$  or  $180^\circ$  where the theoretical patterns are symmetrical forward and backward as shown in Fig. 4.3 (a) based on the analysis of Eq. (4.1). The measured and simulated total efficiency of our design match well as shown in Fig. 4.12. The maximum total efficiency is 67.8% measured at 2.43 GHz. It decays fast as frequency moving away which indicates the high selectivity of the proposed design. The realized gain and total efficiency mentioned in this chapter all take into account the reflection loss due to mismatch.



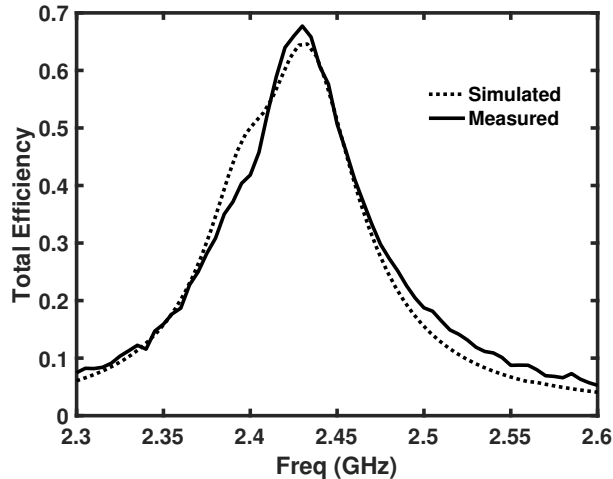


Figure 4.12: Measured and simulated total efficiency of the antenna versus frequency.

#### 4.4 Discussion

The proposed antenna offers endfire radiation with vertical polarization in a very compact structure. In Table 4.2, the antenna itself is compared with some low-profile endfire antennas, including Yagi, Vivaldi, and bowtie dipoles antennas. Our antenna has the smallest size but offers decent endfire gain with vertical polarization. The design reported in [14] also has vertical polarization, but its main beam is not pointing at endfire due to the diffraction of the ground and thus the endfire gain is not so high considering its large size. There are two designs in [14], which are marked as [14]:1 and [14]:2 in Table 4.2, and same for [17]. In Table 4.2, the “Freq” refers to the center frequency, and the “Gain” refers to the endfire gain.

Similar to the regular dipole antenna, the proposed antenna, on the other hand, suffers from the unbalanced current along the coaxial feeding. The common-mode choke is required, which could increase the overall depth, thus limiting the proposed antenna for some applications. One must take it into consideration during the installation.

The proposed antenna also has the advantages of its simple configuration, cheap fabrication, and high selectivity. It is easy to be scaled to different frequency domain, or to be integrated with on-chip or on-board designs. The high selective response of the antenna

Table 4.2: Comparison of low-profile endfire antennas

<b>Endfire Antenna</b>	<b>Freq (GHz)</b>	<b>Overall Size</b>	<b>Gain (dBi)</b>	<b>Polarization (to ground)</b>
Proposed Design	2.41	$0.26\lambda_0 \times 0.44\lambda_0$	2.8	Vertical
[14]:1	5.21	$1.91\lambda_0 \times 2.08\lambda_0$	4 to 6	Vertical
[14]:2	5.21	$1.72\lambda_0 \times 3.43\lambda_0$	7.4 to 10.4	Vertical
[12]	9.5	$0.5\lambda_0 \times 0.5\lambda_0$	3.4 to 5.1	Horizontal
[17]:1	6.85	$0.92\lambda_0 \times 0.97\lambda_0$	$\sim -1$ to 5	Horizontal
[17]:2	6.85	$0.79\lambda_0 \times 0.90\lambda_0$	$\sim -2$ to 5	Horizontal
[20]	8.05	$0.75\lambda_0 \times 1.21\lambda_0$	3 to 5.3	Horizontal

prevents it from undesired off-band crosstalk and thus offers better isolation, which is very useful in some applications. Like patch antenna, the maximum realized gain along with the 3-dB bandwidth and F/B ratio of the proposed antenna could be further improved by increasing the width or height of the design as long as the two coupled modes are not destroyed. Phased array concept can be implemented on top of our design to achieve scanning performance. In conclusion, our design would find applications in the communication systems on a horizontal platform, like chip-to-chip, vehicle-to-vehicle or any on-ground communications.

## 4.5 Conclusion

An endfire coupled-mode patch antenna with vertical polarization along with its design philosophy is presented. The basic idea is to manipulate the phase at the two radiating slots. Besides the phase controlled by even and odd mode, additional phase shift is introduced by the feeding to ensure forward endfire radiation for both modes. The ground

of the antenna is trimmed to eliminate undesired effect on the patterns. The equivalent circuit model of the antenna is built based on the filter theory.

The sample of the antenna is fabricated and demonstrated with well-matched simulated and measured high selective two-pole frequency responses. The simulated patterns, similar to the theoretical ones calculated by the array factor, indicates the endfire radiations within the band despite of slight pattern changing with frequency. However, the common mode current on the outside of the feeding coaxial cable radiates and perturbs the measured patterns as well as the realized endfire gain and total efficiency. Therefore, a quarter-wavelength bazooka balun is applied along the coaxial feeding of the sample. The measured performances, including the patterns on Elevation ( $xz$  plane of cut) and Azimuth ( $xy$  plane of cut) plane, endfire realized gain, F/B ratio, and total efficiency, are good and compare closely with the simulated ones.

The proposed endfire antenna benefits from its vertical polarization, simple and compact configuration, cheap and friendly fabrication, and high selectivity. Since the main beam points to endfire direction, the design offers decent endfire gain in term of its size. With the same design philosophy, the antenna can be easily scaled to different frequencies or integrated with on-chip or on-board designs. The proposed design could find its applications in many communication scenarios.

## CHAPTER 5

# Circularly Polarized HMSIW Antenna

### 5.1 Introduction

Antenna with circular polarization (CP) plays an important role in modern wireless communications. It solves the problem of the polarization mismatch caused by the multipath interference and the wave propagation in ionosphere. CP antenna with microstrip technology has been well studied, and the design procedure is mature [1]. However, microstrip antennas suffer from high conduction loss, which makes them less competitive in the high-frequency domain.

The substrate integrated waveguide (SIW) cavity-based CP antennas have low conduction loss and high gain, while maintaining the advantages of low profile, low cost, and easy integration with planar circuits [21–25]. However, generating pure CP waves in SIW cavities is not as straightforward as that in microstrip patches. The general solutions are either to design two standalone radiating elements [25], or to cut slots on top (or bottom) of the SIW cavity [21–24]. The first solution requires external feeding to provide the phase difference. For the second one, though widely used, the performance of the antennas is highly dependent on the shape, size, and location of the slots. Therefore, the design procedure typically involves heavy optimization in full-wave simulators, which takes a lot of time and computation.

In this chapter, a CP antenna with SIW technique is developed by a fast and robust design methodology, based on the coupled-mode concept[26]. The antenna contains two coupled half-mode SIW (HMSIW) cavities. The even and odd eigen-modes are excited inside the structure, similar to the coupled-mode patch antenna [5, 18, 27]. The design method evolves from filtering theory, where the equivalent circuit model is optimized to

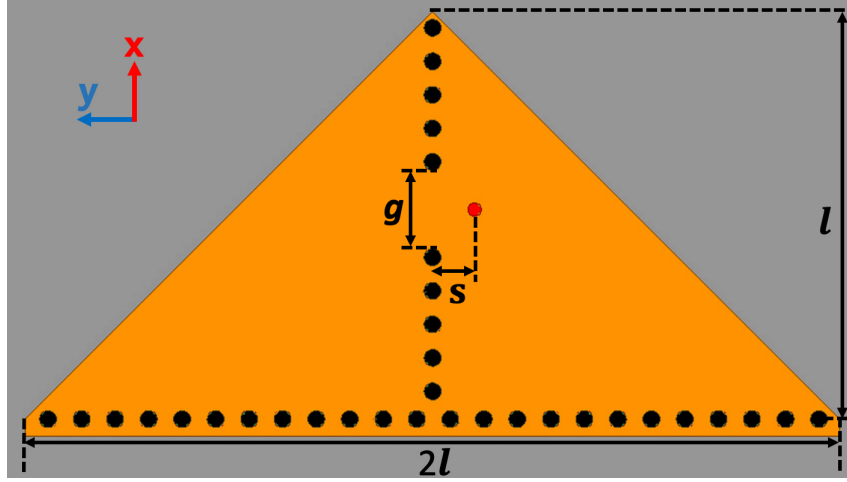


Figure 5.1: Top-view schematic layout of the proposed filtering antenna. The black dots represent the metal via posts connecting top to the ground, whose diameter is 1.6 mm and spacing is 3.2 mm. The red dot is the back-fed probe. The dimensions are all in mm:  $l = 38.9$ ,  $g = 7.5$ ,  $s = 4$ .

realize the target operating frequency and bandwidth. The final structure is directly synthesized from the circuit model, avoiding the heavy optimization in full-wave simulator. The proposed antenna has very low axial ratio (AR) at target frequency while still maintaining decent gain and AR bandwidth. The design procedures, along with the results and discussions, are presented in the following sections.

## 5.2 Design Method and Theory

The schematic layout of the proposed antenna is shown in Fig. 5.1. Two identical HMSIW cavities have orthogonal polarization to each other. A gap on the center wall brings magnetic coupling between the two cavities. Therefore, two eigen-modes, even and odd mode, can be supported. The antenna is back-fed through a coaxial cable to the right side cavity. The feeding breaks the symmetry of the excited modes, so that the radiating wave of the right HMSIW cavity leads the phase within the matching band [27]. As a result, RHCP is the co-polarization of the antenna. The antenna will radiate left handed CP (LHCP) waves if the feeding is symmetrically located to the left side. The design target is

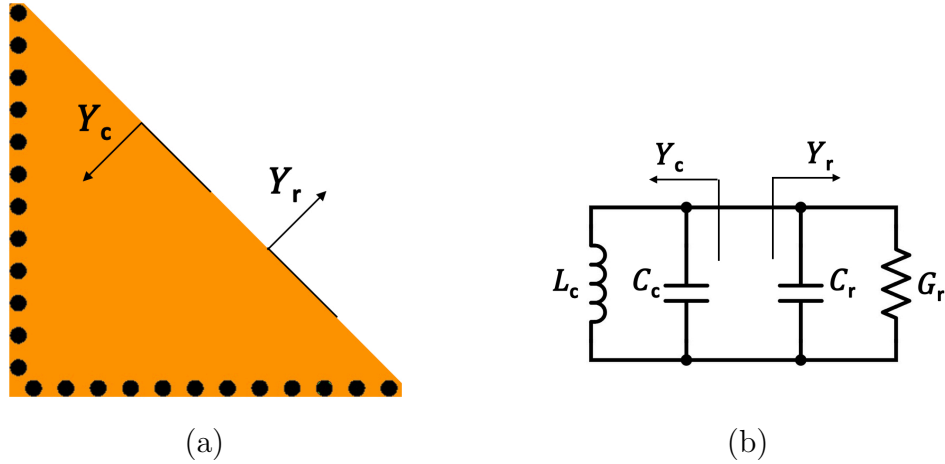


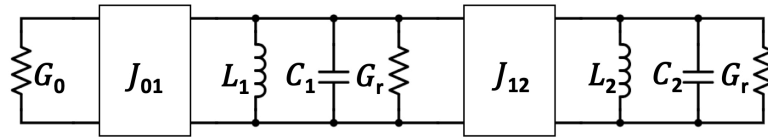
Figure 5.2: (a) HMSIW radiating resonator. (b) Equivalent lumped circuit model for the radiating resonator.

to have CP waves at center frequency of 3.58 GHz and achieve 3% impedance bandwidth. The substrate is a conductor-backed Rogers RT/duroid 5880 with dielectric constant of 2.2 and thickness of 1.57 mm. The design procedure and the theory are demonstrated in the following subsections.

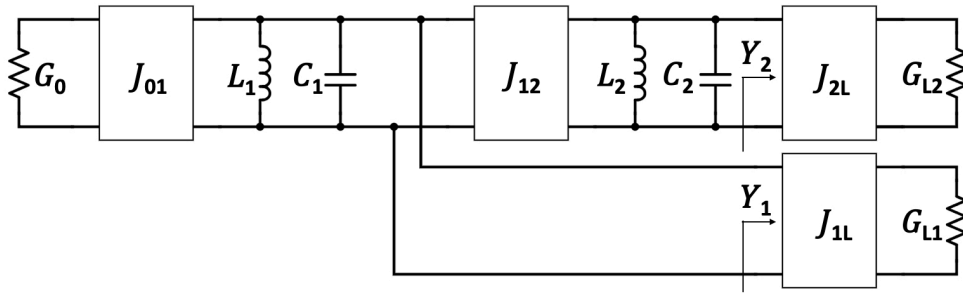
### 5.2.1 Design Procedure

The first step is to build and characterize a HMSIW cavity resonant at target center frequency. The dimension of the cavity can be calculated by the equations [28]. The cavity is characterized by the equivalent circuit model as shown in Fig. 5.2. From the radiating edge to the left, it is a cavity resonator whose input admittance  $Y_c$  is modeled by shunt LC tank,  $L_c$  and  $C_c$  as shown in Fig. 5.2 (b). From the edge to the right side, the fringing field at the edge contributes to the additional capacitance of the cavity resonator and the radiation to the free space. The input admittance  $Y_r$  is thus modeled by shunt capacitance  $C_r$  and radiation conductance  $G_r$ . The values of the components in circuit model can be extracted based on the theoretical equations and HFSS simulator tool [29]. The impedance bandwidth of the whole antenna is limited by the quality factor of each HMSIW cavity, which can be calculated from the circuit model.

The second step is to construct and optimize the equivalent circuit model of the



(a)



(b)

Figure 5.3: Equivalent circuit model loaded with (a) the radiation conductance  $G_r$ , and (b) the standard loads  $G_{L1} = G_{L2} = 0.02 \text{ S}$ . The admittance inverters  $J_{1L}$  and  $J_{2L}$  are inserted in (b), such that  $Y_1 = Y_2 = G_r$ . The values are:  $G_0 = 0.02 \text{ S}$ ,  $J_{01} = 1.29 \times 10^{-3} \text{ S}$ ,  $J_{12} = 3.58 \times 10^{-4} \text{ S}$ ,  $L_1 = L_2 = 0.42 \text{ nH}$ ,  $C_1 = C_2 = 4.71 \text{ pF}$ ,  $G_r = 2.98 \times 10^{-3} \text{ S}$ , and  $J_{1L} = J_{2L} = 1.07 \times 10^{-3} \text{ S}$ .

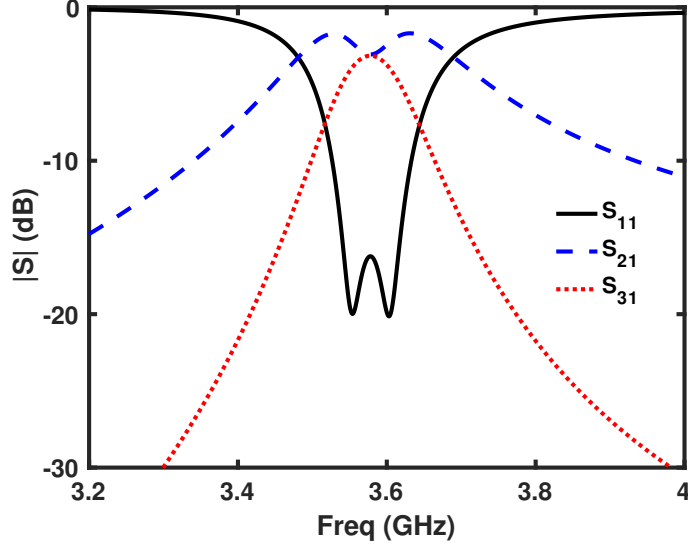


Figure 5.4: Frequency response of the circuit model shown in Fig. 5.3 (b), where  $G_0$ ,  $G_{L1}$ , and  $G_{L2}$  refer to Port 1, 2, and 3 respectively.

whole antenna as shown in Fig. 5.3. In Fig. 5.3 (a), the two identical HMSIW radiating resonators are modeled by the way as discussed previously, where  $C_1 = C_2 = C_c + C_r$ .  $G_0$  represents the source port, the admittance inverter  $J_{01}$  represents the external coupling, and  $J_{12}$  represents the internal coupling. In Fig. 5.3 (b), the model translates the radiation conductance  $G_r$  to an inverter loaded by the standard load, where  $Y_1 = Y_2 = G_r$ . For both models,  $J_{01}$  and  $J_{12}$  are the only two variables that need to be determined.

The circuit model in Fig. 5.3 (b) contains two independent loads,  $G_{L1}$  and  $G_{L2}$ , instead of one single load for regular filters. The two loads represent the radiation of the two HMSIW cavities with orthogonal polarization. The advantage of this model is to provide the delivered power ratio over the frequency. Since the antenna only has one single feed, the input power may not be equally delivered to the two orthogonal radiation loads. In order to get CP waves at target frequency, the three-port circuit prototype has to perform as a 3-dB power divider. Therefore, the internal and external coupling,  $J_{01}$  and  $J_{12}$ , are optimized to have the power equally divided at 3.58 GHz, and to achieve the desired bandwidth. For linear circuit model like the one in Fig. 5.3 (b), the embedded optimizer in ADS can solve the problem efficiently and effectively.



Fig. 5.4 presents the optimized results of the equivalent circuit model.  $S_{21}$  and  $S_{31}$  indicate the power ratio delivered to load  $G_{L1}$  and  $G_{L2}$  respectively, while  $S_{11}$  indicates the input matching. The target 10-dB fractional bandwidth of 3.0% at center frequency of 3.58 GHz is realized. The two nulls in  $S_{11}$  are at 3.55 GHz and 3.60 GHz. The input power is evenly delivered to the two loads at center frequency, since  $S_{21} = S_{31} = -3$  dB. Away from the center frequency, more power is delivered to  $G_{L1}$  than that to  $G_{L2}$ , since the source feeds directly to Resonator 1.

The last step of the design procedure is to design the antenna based on the circuit model. In fact, only the gap in the center wall and the input feeding location need to be designed. Similar to a second-order SIW filter, the gap size is determined by the internal coupling coefficient  $k$ , and the feeding location is determined by the external quality factor  $Q_e$ . The values of  $k$  and  $Q_e$  can be derived from the circuit model by

$$Q_e = \frac{b_1 G_0}{J_{01}^2} \quad (5.1)$$

$$k = \frac{J_{12}}{\sqrt{b_1 b_2}} \quad (5.2)$$

where  $b_i = 2\pi f_0 C_i$  for  $i = 1, 2$  [7]. The gap size and feed location can then be realized with same design methods of resonator filters [30]. Once the gap and feeding are determined, the two orthogonally polarized HMSIW cavities will radiate out equal amount of energy as predicted by the circuit model. However, the circuit model cannot predict the phase difference between the two radiating edges. In the following subsection, we will analyze the eigen-modes and demonstrate that the phase difference is always  $90^\circ$  at the center frequency.

### 5.2.2 Mode Analysis

The even and odd eigen-modes are supported within the structure since the two HMSIW cavities are coupled through the gap in the center wall. Fig. 5.5 illustrates the distributions of the magnitude of E field and the vector of surface current density  $J$  at even and odd

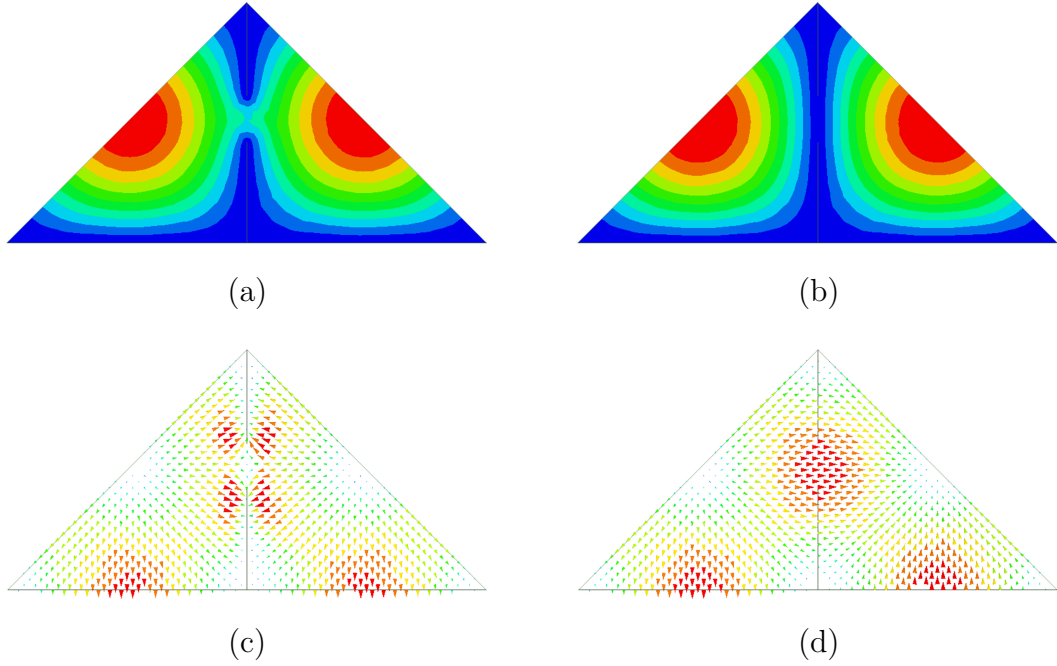


Figure 5.5: Simulated distributions of the complex E field magnitude at (a) even mode and (b) odd mode, and the surface J vector at (c) even mode and (d) odd mode.

modes under eigen-mode simulation in HFSS. Half  $TM_{110}$  mode is supported in each HMSIW cavity resonator as shown in Fig. 5.5 (a) and (b). The vector distributions of surface J in Fig. 5.5 (c) are symmetric to the center wall, which indicates the even mode; while they are antisymmetric in Fig. 5.5 (d), which indicates the odd mode. The fields along the two edges are in-phase at even mode and  $180^\circ$  out-of-phase at odd mode.

The frequencies of the two modes are corresponding to the two nulls of  $S_{11}$ . The lower frequency null is the even mode while the higher one is odd mode, due to the magnetic coupling between the two HMSIW cavities. When the frequency increases from low to high null, the phase difference gradually changes from  $0^\circ$  to  $180^\circ$ . As a result, the phase difference will always be  $90^\circ$  at the center frequency. The input feeding will determine which side of the cavity leads the phase [27]. In our design, the right side cavity is directly fed through the coaxial cable and it then leads the phase. Therefore, the proposed antenna will radiate RHCP waves around the center frequency. Since the two cavities are symmetric, the antenna can be easily modified to radiate LHCP waves by moving the input feeding to the left side cavity. The full-wave simulation are demonstrated

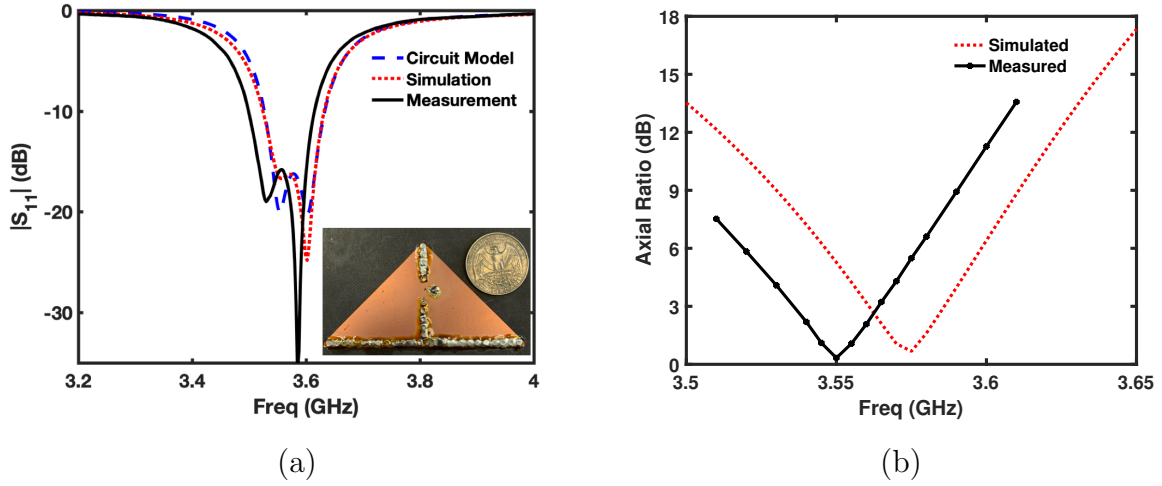


Figure 5.6: Simulated and measured (a)  $S_{11}$  response and (b) Axial Ratio (AR) of the proposed antenna at broadside. The inset figure in (a) shows the fabricated sample.

in Section III along with the measured results.

### 5.3 Antenna Results

Fig. 5.6 shows the simulated and measured  $S_{11}$  and broadside AR of the proposed antenna. The simulated  $S_{11}$  has 3.0% fractional bandwidth with center frequency at 3.58 GHz, identical to the circuit-model  $S_{11}$ . The measured  $S_{11}$  has 3.2% fractional bandwidth with center frequency at 3.55 GHz. The whole band slightly shifts to the lower frequency due to the fabrication tolerance. The measured two nulls are at 3.53 GHz and 3.59 GHz. The simulated broadside AR reaches its minimum of 0.67 dB at 3.58 GHz, as shown in Fig. 5.6 (b). The 3-dB bandwidth of the simulated AR is 0.7%. The measured AR has the 3-dB bandwidth of 0.8% with the minimum of 0.33 dB at 3.55 GHz. The very low AR indicates that the CP waves are well-established by the proposed antenna. The measured and simulated AR closely resemble each other, though the frequency still shifts like  $S_{11}$ .

The surface-J distribution on the top metal of the structure at simulated center frequency is shown in Fig. 5.7 (a). When the current of the right side HMSIW cavity reaches maximum, the current of the left side one is almost zero. This implies that the phase difference between the two radiating edges at the center is indeed  $90^\circ$ . Fig. 5.7 (b) presents

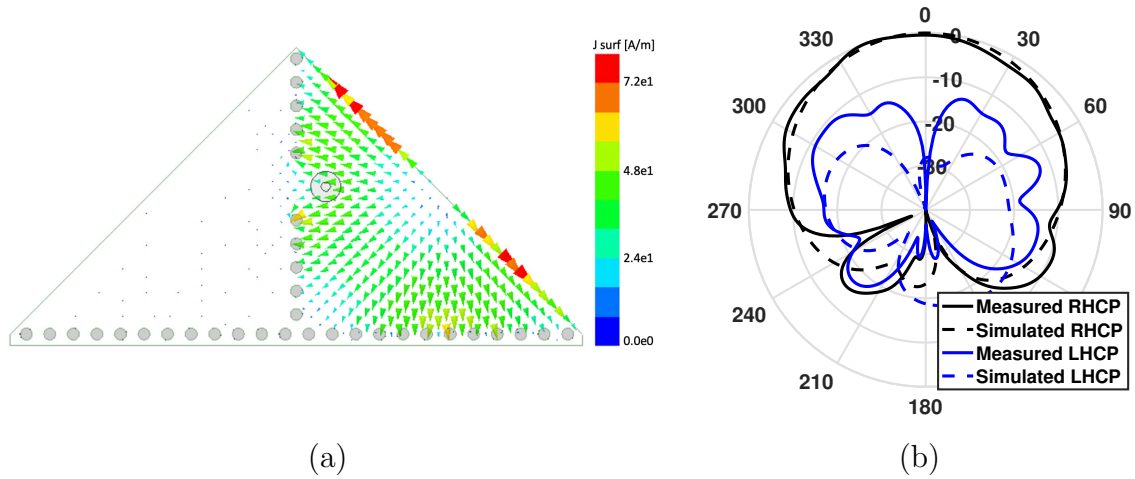


Figure 5.7: (a) Simulated distribution of surface  $J$  at center frequency. (b) Simulated and measured radiation patterns on  $xz$  plane at center frequency.

the radiation patterns of the proposed antenna on  $xz$  plane at center frequency. The simulated and measured results match well with each other. There is a null at broadside of the LHCP pattern, which indicates that the proposed antenna radiates pure RHCP waves there, consistent with the result of AR.

The simulated realized RHCP gain and the radiation efficiency of the proposed antenna are shown in Fig. 5.8. The realized gain and total efficiency discussed in this chapter take the return loss into account. The peak gain of 5.7 dBic is realized at the center 3.58 GHz. The total radiation efficiency within the simulated matching band is around 90%, which indicates the low-loss feature of the HMSIW cavity-backed antenna. The two peaks of the total efficiency curve are corresponding to two matching nulls.

Table 5.1 compares the proposed design with other SIW-based CP antennas. The proposed antenna has the lowest AR, while maintaining comparable AR bandwidth and gain. In addition, the proposed design method of this antenna is fast and robust. The circuit simulator replaces the full-wave simulator for the design optimization to a large extent. As a result, the antenna can be efficiently designed for the specified frequency, impedance bandwidth, and substrate.

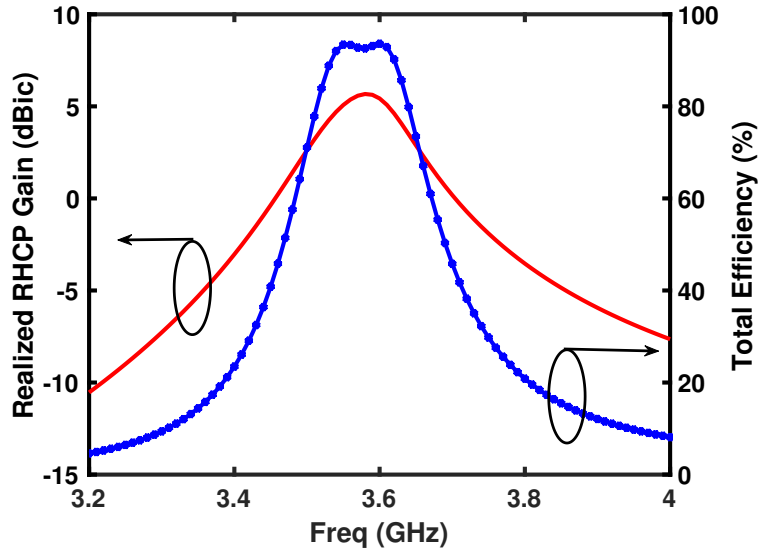


Figure 5.8: Simulated broadside realized gain of RHCP and total efficiency of the proposed antenna.

Table 5.1: Comparison of SIW based CP antennas

SIW CP Antennas	Freq (GHz)	Minimum AR (dB)	AR Bandwidth	Gain (dBic)
This work	3.55	0.33	0.80%	5.7
[21]	10.1	1.1	0.8%	6
[22]	8.75	1.15	0.66%	5.12
[23]	10.2	1.3	2.35%	6
[24]	28	1.2	2.25%	5.3

## 5.4 Conclusion

A CP SIW-based antenna and its design procedure are demonstrated in this chapter. The single-fed antenna contains two coupled HMSIW cavities with orthogonal polarizations. It has very low measured AR with decent gain and bandwidth. The design follows a novel

circuit-model-based design procedure. A three-port equivalent circuit model is built and optimized to realize the target operating frequency and impedance bandwidth. During the design, the circuit simulator replaces the full-wave simulator to a large extent, which makes the procedure more efficient. The proposed CP SIW antenna along the design method is robust and competitive for practical applications.

## CHAPTER 6

# Wide-Band Blazed Grating for All Polarization

### 6.1 Introduction

Blazed structures, which are designed to reflect oblique incident field back to its incident path with very low or even zero specular reflection, have been used in many applications, such as Radar Cross Section (RCS) reduction, frequency scanning reflectors, Littrow mounts, external cavity lasers, and other quasi-optical transmission structures. Traditional 3D structures, like sawtooth (echellette) or groove gratings, are capable of nearly perfect performance but suffer from the bulky structures [31–33]. As an alternative, low-profile gratings have been reported by controlling local phase or resonance realized on regular PCB [34–38]. These designs, however, work for only certain linearly polarized incident fields in general.

Recently, a new resonant blazed surface that works for the incident wave with any polarization has been reported [39]. The design takes square patch on a grounded dielectric substrate as resonator in each unit cell. The patch is first excited by the incident field and then re-radiate to the free space like a regular patch antenna. The square shape of the patch allows the respective responses to two orthogonal polarization, namely TE and TM, which means any phase difference between the two will be maintained. With proper design of the periods later, the all-polarization blazing performance, which is comparable to that of 3D structure, is realized on the finite-size grating. However, the design is limited by the operating bandwidth.

In this chapter, the coupling concept is applied to improve the bandwidth of the original grating design. The coupled square patches are designed in each unit cell and a wide-band planar blazed grating working for all polarization is realized as shown in

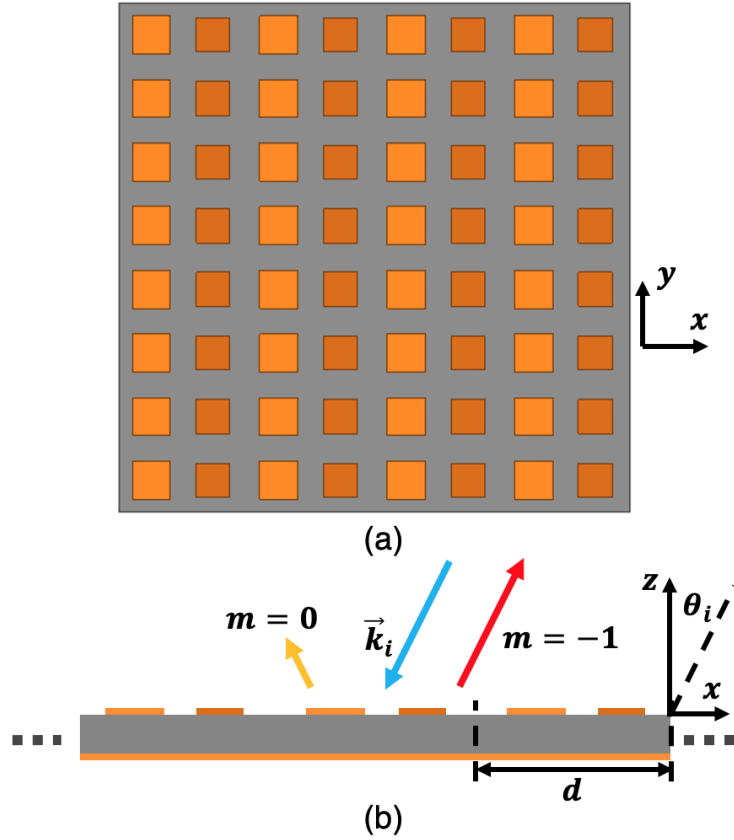


Figure 6.1: (a) A finite grating sample containing 4 by 8 unit cells. The dark and light yellow squares represent the patches in two different sizes. (b) The blazed grating with period  $d$  in x direction scatters the incoming wave (blue) to very low specular  $m = 0$  reflection (yellow) but strong  $m = -1$  diffraction (red).

Fig. 6.1. The square shape contributes to the all-polarization response, while the coupled resonators widen the blazing bandwidth. The frequency response and the field distributions are simulated to demonstrate the operating mechanism. The results of the simulation and measurement of a finite sample show the strong blazing for all polarization within a wide band. The operation and results are presented from a filter perspective.



## 6.2 Operation Mechanism

Fig. 6.1 (b) shows that the blazed surface reflects the incoming wave to  $m = -1$  diffraction order with very low specular reflection. As reported in [40], the system at fixed incident angle can be modeled by a two-port filter network, where the Port 1 and 2 represent the fundamental  $m = 0$  order and the diffraction  $m = -1$  order respectively, and the blazed surface behaves like a bandpass filter. In that sense, if the S parameters is used to show the frequency responses of the surface, the  $S_{11}$  will be the ratio of the specular reflection to the incoming wave, and  $S_{21}$  will be the ratio of  $m = -1$  diffraction to the incoming wave. The later discussion will follow the above definitions.

### 6.2.1 Grating Equation and Bragg Condition

According to Floquet Theory, the operation of a grating for free space propagating waves on the incident plane, x-z plane, is governed by

$$\sin \theta_i + \sin \theta_m = \frac{m\lambda_0}{d} \quad (6.1)$$

where  $\theta_i$  is the incident angle;  $m$  is the diffraction order;  $\theta_m$  is the diffraction angle of order  $m$ ;  $\lambda_0$  is the free-space operating wavelength; and  $d$  is the period of the structure on the incident plane.

In the auto-collimation scenario, where the incident angle is same as the diffraction angle, the grating equation is simplified to Bragg condition, that is

$$k_0 d \sin \theta_i = \pi \quad (6.2)$$

where  $k_0$  is the wave number in free space. The Bragg condition only gives identical angle for certain; however it does not predict a perfect auto-collimation where there is very low or no specular reflection. The design of the unit cell will determine how the scattered energy is distributed between the  $m = 0$  and  $m = -1$  orders. In this case, the unit cell is designed to have nearly perfect auto-collimation in a wide band for any

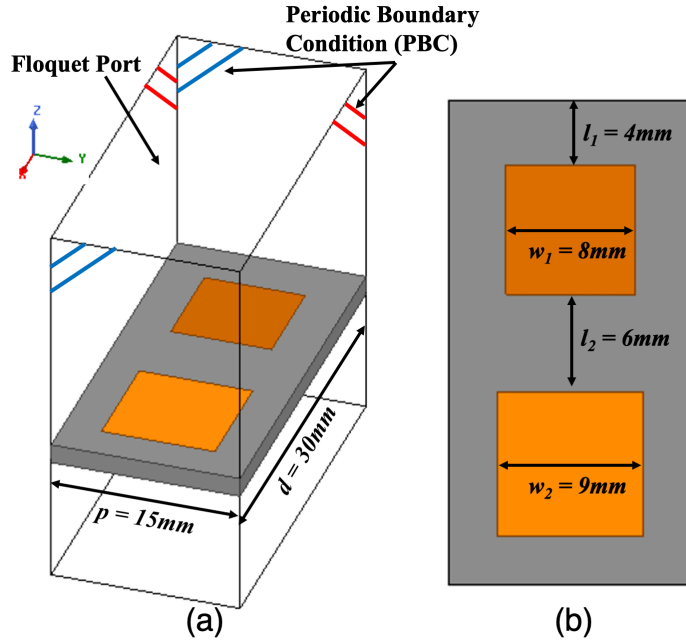


Figure 6.2: (a) Unit cell settings for perfect auto-collimation at  $\theta_i = \theta_{-1} = 30^\circ$ . (b) Top view of the unit cell where two square patches sit on the grounded Rogers RT5880 substrate.

polarization.

### 6.2.2 Unit Cell

Fig. 6.2 shows the unit cell that is built and simulated in HFSS. The Floquet Port with order 0 and  $-1$  harmonics allowed is set as the top excitation, while the periodic boundaries are surrounding on the sides. The period  $d$  along  $x$  direction is chosen to satisfy Bragg condition (6.2) in X band, while the period  $p$  along  $y$  direction is tuned to allow the identical response to both TE- and TM-polarized incidence. Two coupled square patches, with size of 8 mm and 9 mm and separation of 6 mm, are designed to have wide-band all-polarization response.

Fig. 6.3 shows the frequency responses of the unit cell under TE- and TM-pol excitations. As mentioned before, the  $S_{11}$  means the specular reflection and  $S_{21}$  is for the  $-1$  order blazing diffraction. The 3-dB bandwidth extracted from  $S_{21}$  is 18.7%, which

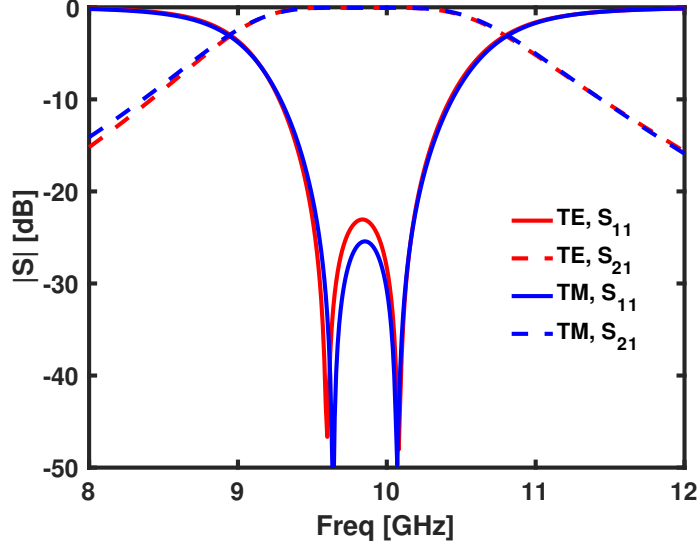


Figure 6.3: Simulated frequency responses with TE- and TM-pol excitations for the unit cell.  $S_{11}$  stands for specular reflection ( $m = 0$ ) and  $S_{21}$  is for  $m = -1$  blazing diffraction.

shows the wide-band response for a infinitely periodic grating consisted by such unit cells. The two-pole responses for both TE and TM are just like traditional two-pole bandpass filter. This is because the coupling is constructed between the two different-size patches to realize the response same as an asynchronously tuned coupled resonator filter. The nearly identical  $S_{11}$  and  $S_{21}$  for TE and TM-pol excitations indicate the all-polarization responses as expected. The location  $l_1$  and separation  $l_2$  of the patches along with the period  $p$  determine the coupling coefficient for TE and TM polarization. During the design, we optimize those parameters to realize identical coupling response for TE and TM cases. An equivalent circuit model can be extracted with proper definitions by applying the methods of filter design [7], which will be left for future discussion.

The simulated magnitude distributions of E field at the poles under TE- and TM-pol excitations are shown in Fig. 6.4. In (a) and (b), the TE polarization excites the fundamental  $TM_{010}^z$  mode in both patches, while for TM polarization,  $TM_{100}^z$  modes are excited as shown in (c) and (d). The two orthogonal modes will re-radiate and contribute to the blazing while maintaining the phase difference of the TE and TM polarization bases. So the grating will work for field with any polarization just like the one reported in

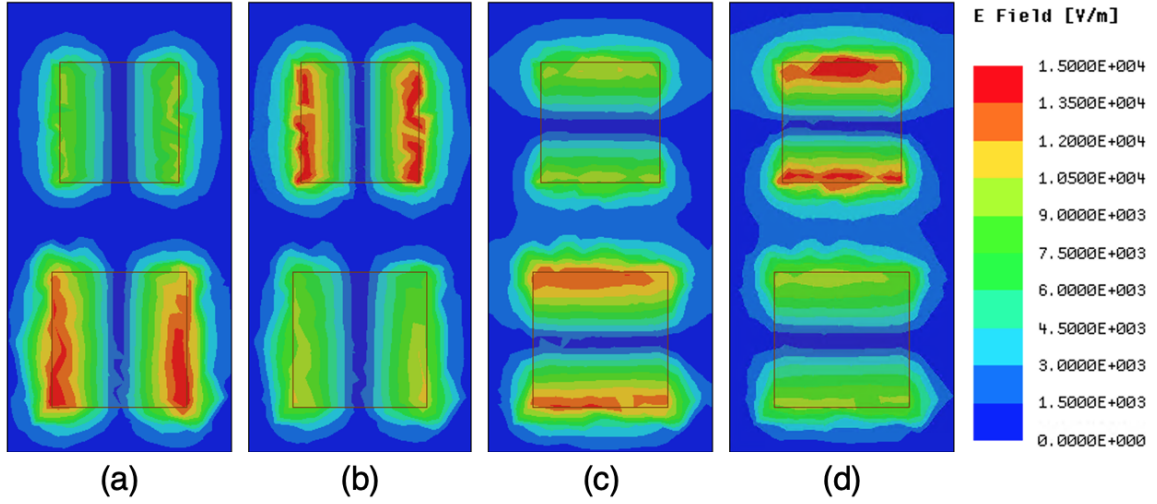


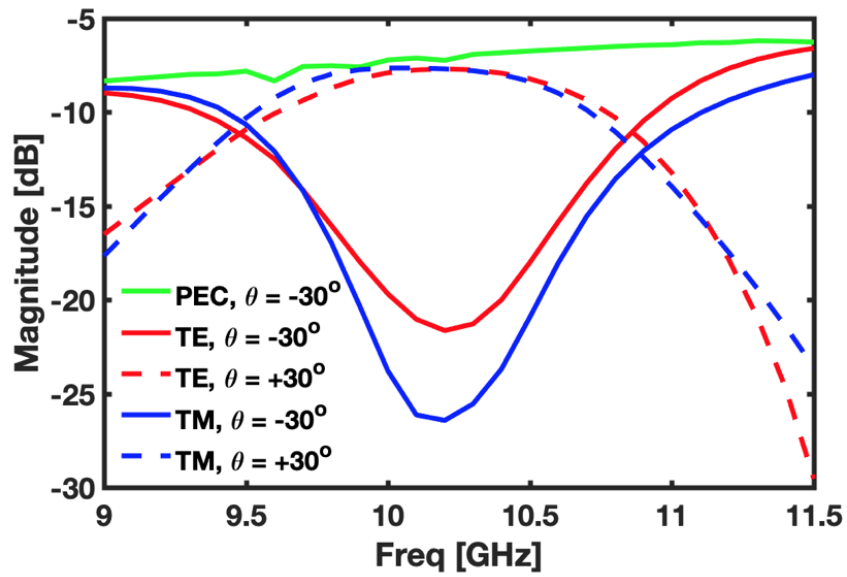
Figure 6.4: Simulated complex E-field magnitude distributions under TE-pol excitation at (a) 9.60 GHz and (b) 10.08 GHz, and TM-pol excitation at (c) 9.64 GHz and (d) 10.07 GHz. The contours of the patches are shown by solid black lines.

[39]. With either polarization, though the fundamental modes of both patches are excited, the larger patch is more strongly excited at lower frequency, while the smaller one is more at higher frequency as shown in Fig. 6.4. This indicates that the coupling exists between the two patches for both polarization and it is expected for the asynchronously tuned coupled resonators [41].

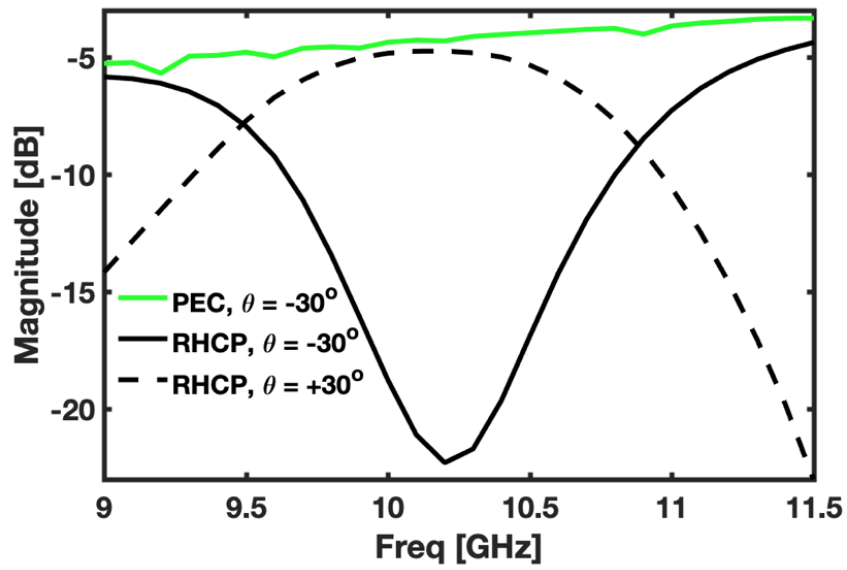
## 6.3 Wide-band Blazed Grating

### 6.3.1 Simulation

A finite grating sample containing 4 by 8 unit cells, as shown in Fig. 6.1 (a), is simulated. Plane waves with different polarization illuminate the sample from incident angle of  $\theta_i = 30^\circ$ . To demonstrate the bandwidth, the magnitudes of scattering E field are plotted at specular reflection angle  $\theta = -30^\circ$  and at incident angle  $\theta = 30^\circ$  (blazing diffraction) versus frequency, as shown in Fig. 6.5. Though results share similar meaning as the S parameter discussed before, they are only about the energy at one angle point. Thus a benchmark has to be set by the specular reflection of a same size PEC under same



(a)



(b)

Figure 6.5: Simulated magnitude of scattering E field at  $\theta = \pm 30^\circ$  for (a) TE- and TM-pol; (b) RHCP incident wave at  $\theta_i = +30^\circ$ . The specular reflection of a same size PEC mirror is simulated as comparison shown by green slot line.

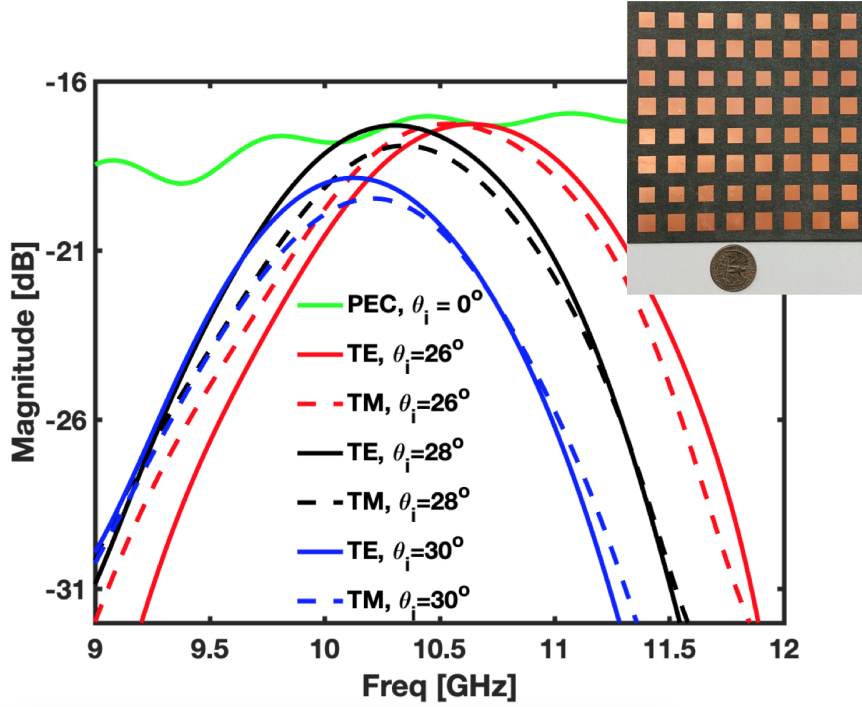


Figure 6.6: Measured auto-collimation results under three incident angles for both TE and TM polarization. The reflection of a same size PEC under normal incident  $\theta_i = 0$  is measured to serve as a benchmark. The inset figure shows the fabricated sample.

illumination. It gives the maximum reflection magnitude one can get by illuminating a passive grating of such size.

The maximum diffractions of the blazed grating under both linear or circular polarization shown in Fig. 6.5 are almost identical to the PEC reflection at the same frequency and polarization, which indicates strong auto-collimation achieved by this design. The simulated 3-dB bandwidth, defined by the response of  $\theta = +30^\circ$ , is 12.8%, similar for all polarization. This indicates the finite grating still works for wide band though the bandwidth is smaller than the infinite grating due to the limited size. The magnitude of scattering field for PEC increases as the frequency increases. This is because in terms of wavelength the mirror size is increasing as frequency, and thus more energy is reflected by the PEC.

### 6.3.2 Measurement

The auto-collimation measurement is carried by a mono-static radar setup where one linear polarized horn antenna serves as both transmitter and receiver. The grating under test (GUT) is on a rotator at the far field region so that the radiation of the antenna can be assumed as plane wave. By rotating the GUT azimuthally, the frequency response can be measured under different incident angles  $\theta_i$ . Time gating method is applied to the measured data in order to get rid of the background noise and thus improve the measurement accuracy.

Fig. 6.6 shows the measured auto-collimation results. Identical responses for TE- and TM-pol indicate the all-polarization function as expected. The maximum blazing at  $\theta_i = 26^\circ, 28^\circ$  are identical to the PEC benchmark, which shows the strong blazing realized by the design. These results also indicate that the design operates in a range of blazing angle, not just one  $\theta_i$ . This is because the coupled patches, as the unit cell, response to a wide band of incoming waves. With fixed period, the wide-band frequency response can be translated to wide range of blazing angle as predicted by Eq. (6.2). The blazing at  $\theta_i = 30^\circ$ , however, is about 3-dB lower than the PEC reflection, due to the fabrication tolerance. The measured 3-dB bandwidth at  $\theta_i = 26^\circ$  is 11.5%, comparable to the simulated one at  $\theta_i = 30^\circ$ . Governed by Bragg condition (6.2), the peak blazing points shift to higher frequency as  $\theta_i$  decreases under the fixed period  $d$ . The sinusoidal-like response of PEC is due to the standing waves under normal incidence. The measurement results overall prove that this design works in a wide band and for all polarization.

## 6.4 Conclusion

A wide-band all-polarization blazed grating is presented. The asynchronously tuned coupled resonators are introduced into each unit cell and design them to work for all polarization. Two-pole frequency responses, similar to a regular bandpass filter, are realized in the unit-cell simulation. Measured and simulated results of the finite grating sample show good performance as expected. The results of this paper indicate that the bandwidth for

such all-pol blazed grating can possibly be further extended by putting more coupled resonators in a properly designed unit cell.



## CHAPTER 7

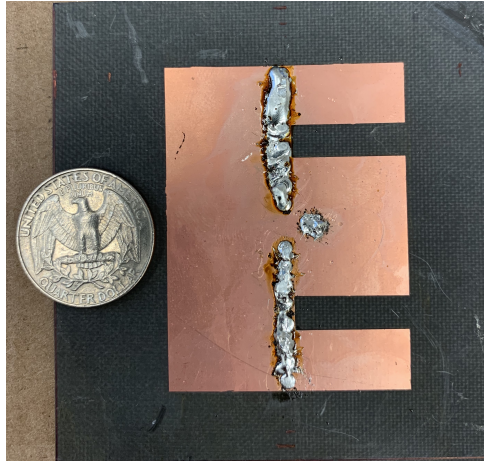
### Conclusion

The concept of coupled modes is developed and applied to compact antenna and reflector array designs. Compact antennas featured with beam steering, endfire radiation with vertical polarization, and circular polarization are demonstrated respectively. A wide-band all-polarization blazing grating array is presented. The proposed design method introduces the new radiation features by taking the advantage of mutual coupling, which in contrast is typically an annoying problem for array designs. The equivalent circuit model derived from filtering concept provides an accurate design guideline which accelerates the simulation procedure. All the proposed designs maintain simple, robust, and cost-efficient.

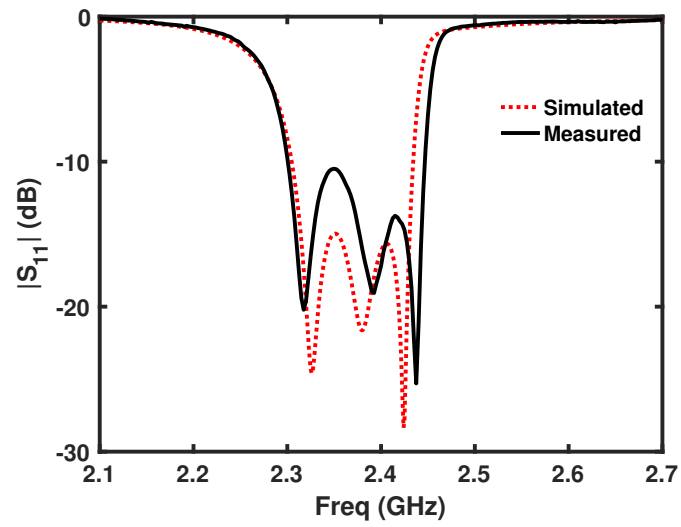
Compatibility is another important advantage of the proposed design concept. The coupled-modes concept can be added on top of many other antenna design methods to improve the original performance or to create new desired feature. To demonstrate the strong compatibility, two examples are briefly introduced in the following paragraphs.

The first example combines the design technique of E-shape patch [42] and coupled-mode concept into a patch antenna [8]. The results and the fabricated sample are shown in Fig. 7.1. By cutting the two slots, additional coupled resonance is brought into coupled-mode patch antenna (CMPA). Compared to the original CMPA, the reported antenna has 36% wider operation bandwidth and 80% more in-band scanning angle range, while remaining simple, robust, and cost-efficient. Many other bandwidth-improvement methods can also be co-designed with coupled-mode concept by following the similar design procedure reported in [8].

The other example is to design phased array with CMPA as single element. A two-endfire-element array with balanced feeding structure reported in [43]. The fabricated

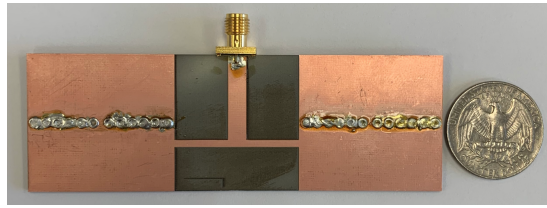


(a)

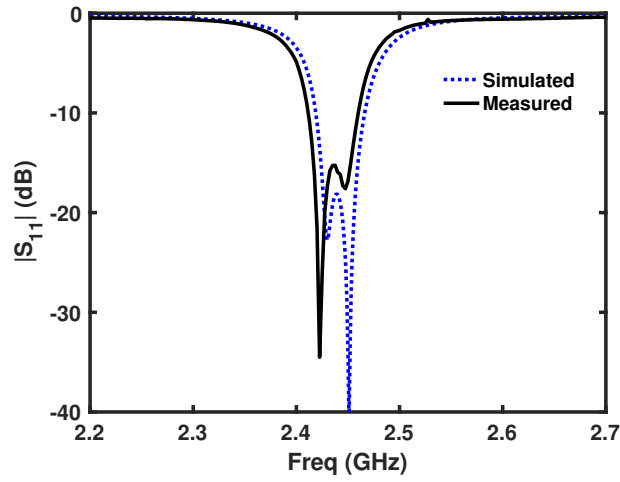


(b)

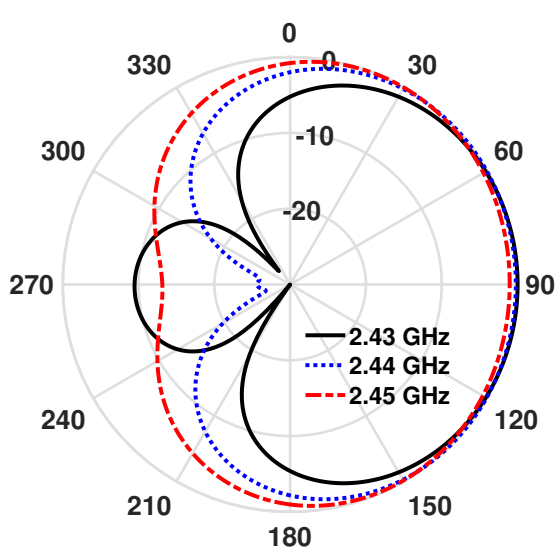
Figure 7.1: (a) Sample of the E-shape CMLPA. (b) Frequency response.



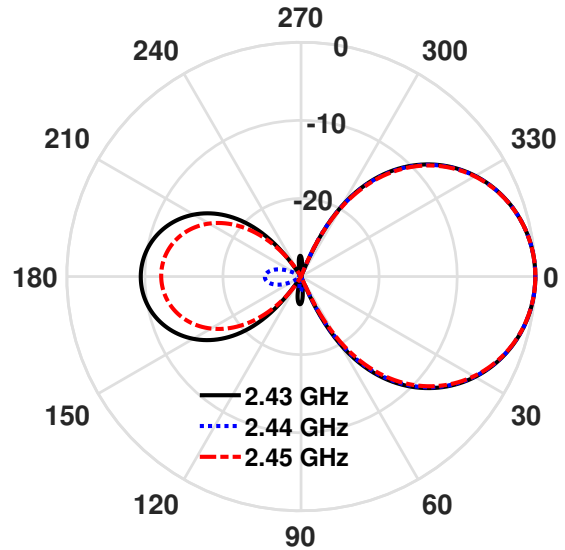
(a)



(b)



(c)



(d)

Figure 7.2: (a) Sample of the two-endfire-element array. (b) Frequency response. Simulated co-pol patterns on (c) Elevation plane and (d) Azimuth plane.

sample and results are illustrated in Fig. 7.2. The array contains two endfire CMPA [27], which are fed by a T-shape parallel plate waveguide (PPWG) power divider. The PPWG feeding provides well-balanced input signal while maintaining low profile. It eliminates the undesired radiation of common-mode current, and thus addresses the major issue for the endfire CMPA. The proposed array has the measured bandwidth of 2.1% centered at 2.435 GHz, and offers 4.6 dBi simulated peak gain at endfire and maximum front-to-back ratio of 23 dB. The proposed array radiates exact endfire patterns with vertical polarization while maintaining compact size and low profile. In addition, the two elements of the array locate perpendicular to the endfire direction on the horizontal plane. As a result, the array is capable to steer the endfire vertically-polarized beam on azimuth plane with some phase-control components, which could be applied in many scenarios.

The proposed coupled-mode concept alleviates the design issues of the compact antennas with unique radiation features. It is further developed and applied in reflector array. The strong compatibility of the proposed concept could potentially benefit more antenna designs. As a conclusion, the proposed concept provides a new antenna design perspective and there are definitely more possibilities to explore in the future.

## REFERENCES

- [1] A. Constantine Balanias, *Antenna Theory: Analysis and Design*, 3rd ed. John Wiley & Sons, 2005.
- [2] L. Liu, C. Caloz, and T. Itoh, “Dominant mode leaky-wave antenna with backfire-to-endfire scanning capability,” *Electronics Letters*, vol. 38, no. 23, pp. 1414–1416, 2002.
- [3] D. R. Jackson, C. Caloz, and T. Itoh, “Leaky-wave antennas,” *Proceedings of the IEEE*, vol. 100, no. 7, pp. 2194–2206, 2012.
- [4] A. K. Bhattacharyya, *Phased array antennas: Floquet analysis, synthesis, BFNs and active array systems*. John Wiley & Sons, 2006, vol. 179.
- [5] H. Tian, K. Dhvaj, L. J. Jiang, and T. Itoh, “Beam scanning realized by coupled modes in a single-patch antenna,” *IEEE Antennas and Wireless Propagation Letters*, vol. 17, no. 6, pp. 1077–1080, 2018.
- [6] Y. Yusuf and X. Gong, “Compact low-loss integration of high- $q$  3-d filters with highly efficient antennas,” *IEEE Transactions on Microwave Theory and Techniques*, vol. 59, no. 4, pp. 857–865, 2011.
- [7] J. S. G. Hong and M. J. Lancaster, *Microstrip filters for RF/microwave applications*, 2nd ed. John Wiley & Sons, 2011.
- [8] H. Tian and T. Itoh, “Coupled-mode patch antenna with improved bandwidth and scanning angle range,” in *2019 IEEE Asia-Pacific Microwave Conference (APMC)*. IEEE, 2019, pp. 1110–1112.
- [9] W. J. Hofer, “Equivalent series inductivity of a narrow transverse slit in microstrip,” *IEEE Transactions on microwave theory and techniques*, vol. 25, no. 10, pp. 822–824, 1977.
- [10] H. Yagi, “Beam transmission of ultra short waves,” *Proceedings of the Institute of Radio Engineers*, vol. 16, no. 6, pp. 715–740, 1928.
- [11] J. Huang, “Planar microstrip Yagi array antenna,” in *Antennas and Propagation Society International Symposium, 1989. AP-S. Digest*. IEEE, 1989, pp. 894–897.
- [12] N. Kaneda, W. Deal, Y. Qian, R. Waterhouse, and T. Itoh, “A broadband planar quasi-Yagi antenna,” *IEEE Transactions on Antennas and Propagation*, vol. 50, no. 8, pp. 1158–1160, 2002.
- [13] G. R. DeJean and M. M. Tentzeris, “A new high-gain microstrip Yagi array antenna with a high front-to-back (f/b) ratio for wlan and millimeter-wave applications,” *IEEE Transactions on Antennas and Propagation*, vol. 55, no. 2, pp. 298–304, 2007.

- [14] J. Liu and Q. Xue, "Microstrip magnetic dipole Yagi array antenna with endfire radiation and vertical polarization," *IEEE Transactions on Antennas and Propagation*, vol. 61, no. 3, pp. 1140–1147, 2013.
- [15] E. Gazit, "Improved design of the Vivaldi antenna," in *IEE Proceedings H-Microwaves, Antennas and Propagation*, vol. 135, no. 2. IET, 1988, pp. 89–92.
- [16] J. Langley, P. Hall, and P. Newham, "Balanced antipodal Vivaldi antenna for wide bandwidth phased arrays," *IEE Proceedings-Microwaves, Antennas and Propagation*, vol. 143, no. 2, pp. 97–102, 1996.
- [17] A. Z. Hood, T. Karacolak, and E. Topsakal, "A small antipodal Vivaldi antenna for ultrawide-band applications," *IEEE Antennas and Wireless propagation letters*, vol. 7, pp. 656–660, 2008.
- [18] H. Tian, L. J. Jiang, and T. Itoh, "A compact single-element pattern reconfigurable antenna with wide-angle scanning tuned by a single varactor," *Progress In Electromagnetics Research C*, vol. 92, pp. 137–150, 2019.
- [19] J. Huang, "The finite ground plane effect on the microstrip antenna radiation patterns," *IEEE Transactions on Antennas and Propagation*, vol. 31, no. 4, pp. 649–653, 1983.
- [20] S.-W. Qu, J.-L. Li, Q. Xue, and C.-H. Chan, "Wideband periodic endfire antenna with bowtie dipoles," *IEEE Antennas and Wireless Propagation Letters*, vol. 7, pp. 314–317, 2008.
- [21] G. Q. Luo, Z. F. Hu, Y. Liang, L. Y. Yu, and L. L. Sun, "Development of low profile cavity backed crossed slot antennas for planar integration," *IEEE transactions on Antennas and Propagation*, vol. 57, no. 10, pp. 2972–2979, 2009.
- [22] S. A. Razavi and M. H. Neshati, "Development of a low-profile circularly polarized cavity-backed antenna using HMSIW technique," *IEEE Transactions on Antennas and Propagation*, vol. 61, no. 3, pp. 1041–1047, 2012.
- [23] D.-Y. Kim, J. W. Lee, T. K. Lee, and C. S. Cho, "Design of SIW cavity-backed circular-polarized antennas using two different feeding transitions," *IEEE Transactions on Antennas and Propagation*, vol. 59, no. 4, pp. 1398–1403, 2011.
- [24] Q. Wu, H. Wang, C. Yu, and W. Hong, "Low-profile circularly polarized cavity-backed antennas using SIW techniques," *IEEE Transactions on Antennas and Propagation*, vol. 64, no. 7, pp. 2832–2839, 2016.
- [25] K. Kim and S. Lim, "Miniaturized circular polarized TE<sub>10</sub>-mode substrate-integrated-waveguide antenna," *IEEE Antennas and Wireless Propagation Letters*, vol. 13, pp. 658–661, 2014.
- [26] H. Tian and T. Itoh, "Development of a circularly polarized HMSIW antenna," *Progress In Electromagnetics Research Letters*, vol. 87, pp. 81–87, 2019.

- [27] H. Tian, L. Jiang, and T. Itoh, "Compact endfire coupled-mode patch antenna with vertical polarization," *IEEE Transactions on Antennas and Propagation*, vol. 67, no. 9, pp. 5885–5891, 2019.
- [28] D. M. Pozar, *Microwave engineering*. John Wiley & Sons, 2009.
- [29] K. Dhvaj, J. M. Kovitz, H. Tian, L. J. Jiang, and T. Itoh, "Half-mode cavity-based planar filtering antenna with controllable transmission zeroes," *IEEE Antennas and Wireless Propagation Letters*, vol. 17, no. 5, pp. 833–836, 2018.
- [30] R. J. Cameron, C. M. Kudsia, and R. R. Mansour, *Microwave filters for communication systems: fundamentals, design, and applications*. John Wiley & Sons, 2018.
- [31] A. Hessel, J. Schmoys, and D. Tseng, "Bragg-angle blazing of diffraction gratings," *JOSA*, vol. 65, no. 4, pp. 380–384, 1975.
- [32] B. H. Kleemann, "Perfect blazing with echelle gratings in TE and TM polarization," *Optics letters*, vol. 37, no. 6, pp. 1002–1004, 2012.
- [33] W. Chen, N. Beaulieu, D. Michelson, and E. Jull, "Off-bragg blazed rectangular groove gratings for high diffraction efficiency devices," *IEEE Transactions on Antennas and Propagation*, vol. 61, no. 4, pp. 2342–2347, 2013.
- [34] X. Li, M. Memarian, K. Dhvaj, and T. Itoh, "Blazed metasurface grating: the planar equivalent of a sawtooth grating," in *Microwave Symposium (IMS), 2016 IEEE MTT-S International*. IEEE, 2016, pp. 1–3.
- [35] A. M. Wong, P. Christian, and G. V. Eleftheriades, "Binary Huygens' Metasurfaces: Experimental Demonstration of Simple and Efficient Near-Grazing Retroreflectors for TE and TM Polarizations," *IEEE Transactions on Antennas and Propagation*, vol. 66, no. 6, pp. 2892–2903, 2018.
- [36] C. Tao, M. Memarian, Y. Morimoto, and T. Itoh, "Non-periodic metasurfaces for blazing and beam splitting," in *Microwave Conference (APMC), 2016 Asia-Pacific*. IEEE, 2016, pp. 1–4.
- [37] M. Memarian, X. Li, and T. Itoh, "Resonant blazed metasurface gratings," in *Microwave Conference (EuMC), 2016 46th European*. IEEE, 2016, pp. 297–300.
- [38] H. Tian, M. Memarian, and T. Itoh, "Electronically-tunable resonant blazed metasurface grating," in *Microwave Conference (APMC), 2017 IEEE Asia Pacific*. IEEE, 2017, pp. 376–379.
- [39] H. Tian and T. Itoh, "All-polarization blazed surface," in *Microwave Conference (APMC), 2018 IEEE Asia Pacific*. IEEE, 2018.
- [40] M. Memarian, X. Li, Y. Morimoto, and T. Itoh, "Wide-band/angle blazed surfaces using multiple coupled blazing resonances," *Scientific Reports*, vol. 7, p. 42286, 2017.
- [41] R. J. Cameron, C. M. Kudsia, and R. Mansour, *Microwave filters for communication systems*. John Wiley & Sons, 2015.

- [42] F. Yang, X.-X. Zhang, X. Ye, and Y. Rahmat-Samii, “Wide-band e-shaped patch antennas for wireless communications,” *IEEE transactions on antennas and propagation*, vol. 49, no. 7, pp. 1094–1100, 2001.
- [43] H. Tian and T. Itoh, “Endfire coupled-mode patch antenna array with balanced feeding,” in *Microwave Conference (EuMC), 2020 European*. IEEE, 2020 (accepted).